ADVANCED MATERIALS

Supporting Information

for *Adv. Mater.,* DOI: 10.1002/adma.202206956

Voltage-Modulated Untwist Deformations and Multispectral Optical Effects from Ion Intercalation into Chiral Ceramic Nanoparticles

Xiao Shao, Cheng Zhu, Prashant Kumar, Yanan Wang, Jun Lu, Minjeong Cha, Lin Yao, Yuan Cao, Xiaoming Mao, Hendrik Heinz, and Nicholas A. Kotov**

Supplementary Materials

Voltage-Modulated Untwist Deformations and Multispectral Optical Effects from Ion Intercalation into Chiral Ceramic Nanoparticles

Xiao Shao,[1,2,3] Cheng Zhu,[4] Prashant Kumar,[1,2] Yanan Wang,[1,2] Jun Lu,[1,2] Minjeong Cha,[2,5] Lin Yao,[1,2] Yuan Cao,[1,2] Xiaoming Mao,[5] Hendrik Heinz,[4]* Nicholas A. Kotov[1,2,6]*

*Corresponding author. Email: hendrik.heinz@colorado.edu, kotov@umich.edu

This file includes:

Materials and Methods

Chemicals. Vanadium (III) chloride (VCl_3, 97%), *L*-, *D*- and *rac*-tartaric acid (TA, 99%), sodium hydroxide (NaOH, 97%), *L*- and *D*-penicillamine (Pen, 99%), poly (acrylic acid) (PAA, M_w~250 000, 35 wt.% in H_2O), poly(diallyldimethylammonium chloride) (PDDA, M_w 400,000-500,000, 20 wt.% in H_2O), carbon nanotube, single-walled (CNT, 98%), poly (vinylpyrrolidone) (PVP, M_w = 55,000), iron chloride ($FeCl_3$, 97%), zinc sulfate ($ZnSO_4$, 2 M in H_2O, pH 4.2), zinc foil (Zn, 0.25 mm thickness, 99.9%), ethyl alcohol, acetone, isopropanol, and ethylene glycol of reagent grade were all purchased from Sigma-Aldrich. *L*- and *D*-malic acid (MA, 99%) were purchased from Alfa-Aesar. Silver nitrate ($AgNO_3$, 99.95%) was purchased from Fisher Chemical Co.

Synthesis of chiral vanadium oxide nanoparticles (NPs). Vanadium oxide NPs were synthesized by arrested hydrolysis of VCl_3 in water at different pHs in the presence of *L*-, *D*-, and *rac*-TA that served as surface ligands on the NPs. Specifically, 0.128 g VCl_3 and 0.18 g *L*- or *D*-TA were dissolved in 60 mL E-pure water producing a solution with pH 1.4. Using 2.5 M

NaOH, pH was adjusted from 2 to 12 by adding 5 mL aliquots. Then, the solution was incubated at room temperature for one hour with magnetic stirring. A similar process of NP synthesis was used for other chiral ligands, such as MA (0.16 g in 60 mL E-pure water) or Pen (0.18 g in 60 mL E-pure water), producing stable transparent dispersions in all cases.

Preparation of chiral V_2O_3 films. Following a process similar to that described above, 0.128 g VCl_3 and 0.18g *L*- or *D*-TA were added to 30 mL E-pure water, adjusting pH to 3, followed by 1 hour of incubation at room temperature with stirring. The precipitate was obtained by adding two times of volume of isopropanol, and centrifuged at 3000 rpm for 5 min. Finally, the precipitate was re-dissolved in 4 mL water to prepare an aqueous dispersion for film deposition. An ITO substrate was cleaned sequentially with ethyl alcohol, acetone, isopropanol, and water each for 20 min in an ultrasonic bath, then were rinsed with copious amounts of water and dried. Films were cut into 1×3.5 cm^2 segments to fit the sample compartment of the CD spectrometer. To make the coating optically uniform and transparent, NP layers were deposited using layer-by-layer (LBL) assembly. Polarization-active chiroptical film from V_2O_3 NPs were prepared by alternately exposing the ITO-coated glass to positively charged PDDA and negatively charged PAA, charged polymers combined with V_2O_3 NPs. The multilayer films were prepared by alternatively dipping ITO substrates in 0.5% w/v PDDA (0.5% w/v in water) and V_2O_3/PAA (PAA 6.0% w/v in water, 2 mL mixed with 4 mL NPs dispersion) solutions with intermediate double 1-min long immersions in pure water at pH 7. The nanoscale coating obtained after electrostatically restricted adsorption of PDDA and V_2O_3/PAA components will be denoted as a bilayer. The bilayer depositing cycle was repeated as many times as needed procedure to obtain a desired number of multilayers. Typically, each step was analyzed by UV-vis spectra.

The advantage of LBL, over, for instance, spin coating, dip coating, or vacuum assisted filtration is that it results in high and uniform loading of inorganic phase in the composite layer, which is difficult or impossible achieve by other methods. Additionally, the layered method enables higher charge transport due to ability of the NPs to self-assemble as the films are being made promoting formation of percolating charge transport networks [37,38]. LBL also affords seamless integration of different components into the composite films to achieve desirable combination of properties. Note also that unlike batteries where vanadium oxide composites, can also be used, chiroptically active films require high transparency; this essential property is much easier to achieve with LBL due to prevention of agglomeration of NP in each layer. Finally, mechanical properties are also critical for electroactive thin films based on intercalation. The past studies on LBL-engineered coatings indicate that they display required strength, toughness, and adhesion to undergo long-term cycling [39,40].

Preparation of chiral V_2O_3/CNT films. 100 mg of CNT were added to 100 mL solution of 1 mg/mL PAA and dispersed by ultrasonication for 25 min. After centrifugation (6000 rpm, 10 min), 1 mL supernatant with dispersed CNTs was taken out in a separate vial and mixed with 4

mL above V_2O_3 NPs dispersions in water prepared as described above followed by 10 min ultrasonication. Then the homogeneous V_2O_3/CNT solution was added into 2 mL PAA (6.0% w/v in water) solution, followed by 20 min ultrasonication. The process of LBL assembly used for V_2O_3/CNT film was identical to those for V_2O_3 film.

Preparation of chiral V_2O_3/Ag NWs films. Ag NWs were synthesized by a modified polyol process [41,42]. Briefly, 0.2 g of PVP (M_w =55,000) mixed with ethylene glycol (25 mL) were incubated at room temperature under stirring until PVP completely dissolved. Next, $AgNO_3$ (0.25 g) was added to the PVP solution. 3.25 g ethylene glycol solution ($FeCl_3$, 600 µM) was added to the aforementioned reaction mixture with stirring for 1 min. Finally, the mixture was immediately transferred into an oil bath, heated for 1 hour at 130 °C, and then allowed to cool to room temperature under ambient atmosphere. The as-synthesized Ag NWs were washed with water several times to remove the reagent residues and byproducts. The NWs was dispersed into water for further procedures. The Ag NWs with a length of 15-40 µm and a diameter of ~100 nm were synthesized as a component of the composite films to increase the conductivity (Fig. S1A). Their UV absorption peaks were located at 351 nm and 382 nm and therefore did not interfere with the visible and NIR absorption properties of V_2O_3 NPs (Fig. S1B).

The Ag NWs dispersion ($Abs_{600\ nm}$ ~ 2.0, 1 mL) was mixed with 4 mL chiral V_2O_3 solution, followed by 10 min ultrasonication. Then the homogeneous V_2O_3/Ag NWs solution was added into 2 mL PAA (6.0% w/v in water) solution. Identical LBL assembly process as for the previous multilayers was used.

Electrochemical measurements. The electrochemical properties of chiral V_2O_3 ITO film (working electrode) was investigated against a Zn foil counter (reference) electrode in a two electrode system in $ZnSO_4$ solution electrolyte. The cyclic voltammetry was performed using a scan rate of 0.1V/s in a potential window of 0.4-1.8 V (vs. Zn/Zn^{2+}).

Cyclic de/intercalation of NPs films. To monitor the CD spectrum of chiral nanocomposite film, the in-situ CD test with applied voltage was set up (Fig. S2). By changing the current direction, the Zn^{2+} ions can reversibly be inserted and extracted from the film, resulting in the corresponding reversible voltage driven chiroptical activity. The $ZnSO_4$ in H_2O with a concentration of 2 M, pH 4.2, was chosen as the electrolyte. During the intercalation process, the negative electrode of the voltage source was connected to the ITO substrate with multilayers and the positive electrode was connected to the Zn foil. Deintercalation was achieved by reversing the voltage. The applied voltages were maintained at 1 and 1.8 V for Zn^{2+} ions intercalation and deintercalation, respectively. The amount of Zn^{2+} ion insertion depends on the total duration of the charging cycle and the voltage applied. To establish the maximum polarization modulation for the prepared films, the voltage driven process continued to saturation. We rinsed the films with water every 10 cycles to remove surface zinc-based hydroxyl complexes. We found that drying the film (in 60 ºC oven for 5 min) also increased the number of cycles by slowing down the dissolution rate of interfacial contact between the film

and electrolyte. After reducing the amount of intercalated Zn^{2+} into the film, we can achieve longer cycles.

Zn-intercalated *L*-NPs at pH 3, 7 and 11. Ion intercalation in dispersions was accomplished by adding 0.5 mL, 0.5 mL, and 1mL 2M $ZnSO_4$ solution to the 10 mL V_2O_3 NPs followed by one hour of magnetic stirring.

Models for Molecular Dynamics (MD) Simulations. All-atom models for V_2O_3, TA, sodium/chloride ions, and water molecules (flexible SPC water model), were prepared using the *Materials Studio* software package. The INTERFACE Force Field (IFF) parameters were assigned for V_2O_3 models, Zn^{2+}, and sulfate, and CHARMM36 parameters were utilized for to TA molecules. IFF is based on a classical Hamiltonian, including parameters for inorganic and organic compounds with systematic validation of bonding, structure, and energy [18]. The IFF parameters utilized a standard energy expression of class I force fields in CHARMM format.[43,44] The energy terms include a 12-6 Lennard-Jones potential and Lorentz-Berthelot combination rules:

$$E_{pot} = \sum_{ij\ bonds} K_{r,ij}(r_{ij} - r_{0,ij})^2 + \sum_{ijk\ angles} K_{\theta,ijk}(\theta_{ijk} - \theta_{0,ijk})^2 + \sum_{\substack{ijkl\ torsions \\ (in\ plane)}} K_{\phi,ijkl}[1 + cos(n\phi_{ijkl} - \phi_{0.ijkl})] + \sum_{\substack{ijkl\ impropers \\ (out\ of\ plane)}} K_{\chi,ijkl}[1 + cos(n \cdot \chi - \chi_{0.ijkl})] + \frac{1}{4\pi\varepsilon_0\varepsilon_r}\sum_{\substack{ij\ Coulomb \\ (1,2\ and\ 1,3\ excl)}} \frac{q_i q_j}{r_{ij}} + \sum_{\substack{ij\ VDW \\ (1,2\ \ and\ 1,3\ excl)}} \varepsilon_{0,ij}\left[\left(\frac{r_{min,ij}}{r_{ij}}\right)^{12} - 2\left(\frac{r_{min,ij}}{r_{ij}}\right)^{6}\right] \quad \textbf{(1)}$$

We utilized a non-bonded model to describe the inorganic core of the NPs due to predominantly ionic character of chemical bonding in V_2O_3 (Table S2), (1) which precisely reproduces the bond length (over 99.6% accuracy) and lattice parameters (over 99.9% accuracy), and (2) can be easily adapted to surface modifications of hydroxides. To model V_2O_3 NPs, a spherical, stoichiometric V_2O_3 structure with a radius of 14 Å was initially generated from an infinite V_2O_3 crystal. The obtained V_2O_3 core structure was subsequently annealed to 4000 K and cooled down to 298.15 K (decay constant of 1) in vacuum using canonical ensemble (NVT) condition for 8 ps. A relaxed sphere-like structure of minimum energy, composed of 292 V atoms and 438 O atoms (V:O = 2:3), was adopted as the crystalline core structure for MD studies.

The V_2O_3 nanoparticle model was further modified on the surface according to different pH conditions, considering the known chemistry of vanadium in aqueous solution and pK_a of acidic groups (Fig. S9) [45]. The representation of surface chemistry as a function of pH is similar as previously introduced for silica and hydroxyapatite and utilizes experimental data [46]. Accordingly, there are four typical hydrated structures for V(III) in aqueous solution: $[V(H_2O)_6^{3+}]$ with pK_a 2.6, $[V(H_2O)_5\ (OH)^{2+}]$ with pK_a 4.2, and $[V(H_2O)_4(OH)_2^{+}]$ with pK_a 7.0.

At pH above 7, the preferred composition is $[V(H_2O)_3(OH)_3]$. Three representative pH values were selected for the simulations, pH 2.8±0.2 (corresponding to NPs pH 3 and the hydrated structure $V(H_2O)_5(OH)^{2+}$), pH 6.0±0.2 (corresponding to NPs pH 7 and the hydrated structure $V(H_2O)_4(OH)_2^{+}$), and pH 8.0±0.6 (corresponding to NPs pH 11 and the hydrated structure $V(H_2O)_3(OH)_3$). NPs at pH 3 had a crystalline V_2O_3 core with diameter of 12 Å (188 V atoms and 282 O atoms) and a non-crystalline outer hydrated shell with 104 OH groups and 104 V atoms in the form of $V(OH)^{2+}$. For NPs at pH 7, the core structure remained the same as that for NPs at pH 3, and the main species on the V_2O_3 NPs surface was $V(OH)_2^{+}$. Thereby, all exposed surface oxide atoms reacted with water and were changed into two OH groups, including an extra OH group added for each surface V atom to maintain charge neutrality. The outer non-crystalline shell consisted of 199 OH groups and 101 V atoms. Meanwhile, for NPs pH 11, the crystalline V_2O_3 particle core was larger due to larger particle size (292 V atoms and 438 O atoms). In this case, an amorphous $V(OH)_3$ shell with thickness of ~5 Å was added. Herein, the outer layer was composed of 579 OH groups and 193 V atoms. Finally, all NPs model with appropriate surface chemistry were annealed to 4000 K and cooled down to 298.15 K (decay constant of 1) in vacuum using MD simulations in the canonical ensemble (NVT) for 8 ps to obtain representative, equilibrium NP structures. The final radii of the NPs were around 13, 13, and 18 Å for NPs pH 3, 7, and 11, respectively, and thereby similar to the average particle sizes reported by TEM. Though the radius of the NPs pH 11 was slightly larger due to the significant rearrangement size and dynamics of the amorphous shell, it remained within the size distribution from TEM.

Similarly, TA molecules have pK_a values at which the carbonic acid groups will deprotonate into COO^{-}. For *L*-TA, the pK_a values are 2.93 and 4.23, while those for *D*-TA are 2.98 and 4.00 [47]. In summary, the tartaric acid species present in contact with NPs at pH 3, 7, and 11 were $[V(H_2O)_5(OH)^{2+}]/H_2T+HT^{-}$, $[V(H_2O)_4(OH)_2^{+}]/T^{2-}$, and $[V(H_2O)_3(OH)_3]/T^{2-}$, respectively.

The corresponding TA molecules and NP models at specific pH were then placed into the center of a periodic simulation box with size of 65×65×64 $Å^3$, distributing the TA molecules evenly in the residual space. Counter ions such as sodium or chloride ions were added in order to keep the whole system charge neutral. All the NP models were immersed into 6134 flexible SPC water molecules along with 22 molecules of the appropriate TA species, which accurately reproduced the experimental TA concentration of 0.2 M.

Zn intercalation models. We utilized nanoparticles at pH 11 as examples to investigate the intercalation of Zn^{2+} ions. Hereby, we assume partial stoichiometric replacement of Zn inside V_2O_3, which involves two substitutional defects of Zn versus V and removal of one O atom to create an oxygen vacancy per formula unit of V_2O_3 (V_2O_3 (s) + 2 Zn^{2+} (aq) + SO_4^{2-} (aq) + H_2O → 2 ZnO (s) + 2 V^{3+} (aq) + 2 SO_4^{2-} (aq) + 2 OH^{-} (aq)). The Zn ions likely have some added mobility due to the presence of oxygen vacancies and the formation of Frenkel defects was

observed (some dislodging of Zn^{2+} and O^{2-} ions relative to ideal lattice positions). To achieve a Zn intercalation ratio of 10% in the V_2O_3 core, 68 V atoms were substituted by Zn atoms, and subsequent O vacancies were created by removing 34 neighboring O atoms. Due to the Zn substitution and creation of O vacancies, Frenkel defects formed in the models.

The Zn NPs models were then placed into the center of a periodic simulation box with a size of 65×65×65 $Å^3$, with adsorbed 14 TA molecules on the NPs surface using previous simulations in aqueous solutions. Zn^{2+} and SO_4^{2-} ions were added into the simulation box to reproduce the electrolyte with a concentration of 2 M using IFF parameters for sulfate and Zn^{2+} ions [48].

Molecular Dynamics (MD) simulation protocols to analyze NP structures in water. We utilized the Nanoscale Molecular Dynamics (NAMD) program to carry out all MD simulations of adsorption and ion substitution [49]. The typical simulation protocols included a brief geometry optimization to avoid atomic close contacts (200 to 1000 steps), followed by a simulation time of 1 ns for equilibration using the isothermal-isobaric ensemble (NPT) at room temperature and 1 atm pressure. Then, we carried out MD simulations in the NVT ensemble for 20 ns under periodic boundary conditions to sample conformations and energies, using average box dimensions corresponding to 1 atm pressure. Snapshots in the trajectory were collected every 10 ps, we used a simulation time-step of 1 fs, a PME tolerance of 1×10^{-6} and a summation of Lennard-Jones interactions with a spherical cutoff at 1.2 nm. The temperature was maintained at 298.15 K for both NPT and NVT, consistent with the experimental conditions.

Molecular Dynamics (MD) simulation protocols for VCD spectra. To simulate VCD spectra, the initial configurations were derived from the equilibrated structure in solution simulations without water molecules and non-adsorbed TA molecules since VCD spectra were recorded in the dried state (without water) in experiments. The simulations were performed under NVT condition for 20 ps each time with both time-step and trajectory frequency of 1 fs. Other settings remained the same as the equilibrium simulations. The VCD spectra were generated from the trajectory using self-developed Python code with MD analysis using the principles from previous reports [50–52]. More than 50 iterations were made to obtain high quality VCD spectra due to the dynamics of the interfaces and need for averaging over time.

Calculation of the weighted Osipov-Pickup-Dunmur (wOPD) chirality measures. There are multiple chirality measures that one can use to evaluate mirror asymmetry of the geometrical objects. Here took advantage of the one suggested by Osipov, Pickup and Dunmur[21] because it has a specific sign – positive or negative that changes between the left-and right isomers. While being mindful of the problems related to such measures,[22,53] often referred to as pseudoscalar, their careful application can be insightful.[23]

Strictly speaking, all the classical chirality measures, including OPD, are calculated for abstract geometrical points that are specified only by coordinates in the Euclidian space. Their weighted analogs that include molecular/atomic weights of the points, enable one to better account for chemical differences between various chiral states and configurations. Thus here we

computed weighted Osipov-Pickup-Dunmur chirality measures (wOPD) using MD data as inputs. In doing so we separated NPs into two parts – the surface atoms and internal atoms. Only the surface atoms (V, O, and H) were used for the calculations of wOPD because they are (1) affected the most by the chirality transfer from TA surface ligands and (2) most relevant to the untwist deformations. Additional benefit of such approach is marred acceleration of the calculations. The radius of the exempted inner sphere is 9, 9.5, 13, and 14 Å for pH 3, 7, 11, and Zn^{2+} intercalation at pH 11, respectively.

For the same reasons, we also did not include *L/D*-TA molecules in the calculations due to the dynamic nature of the local bonds and molecular positions that would need to be averaged in time. While possible, the benefits of such heavy calculations are not transparent at the moment because the optical effects in visible, red and near infrared windows of the spectrum are associated with chirality of V_2O_3, not with TA.

We coarse-grained surface atoms by grouping them in groups of seven selecting the nearest neighbors from atomic coordinates. Per each group of atoms, the values of wOPD were calculated with the corresponding atomic vector coordinates (*r*) and mass (*w*). A weighted sum of all possible permutation of the four points, corresponding to the coarse-grained 'beads' were calculated according to the following equation [21 54]:

$$wOPD = \frac{4!}{N^4}\frac{1}{3}\left[\sum_{\substack{all\ permunation\ of \\ i,\ j,\ k,l=1\cdots N}} w_i w_j w_k w_l \times \frac{[(r_{ij}\times r_{kl})\cdot r_{il}](r_{ij}\cdot r_{jk})(r_{jk}\cdot r_{kl})}{(r_{ij}r_{jk}r_{kl})^n r_{il}{}^m}\right],$$

where $w_i, w_j, w_k,$ and w_l are the sums of atomic weights of the grouped atoms, $r_i, r_j, r_k,$ and r_l are the vectors determining their location in the Euclidian space, and $r_{i,j}$ and similar notations are the vectors between the 'beads' *i* and *j*.

Characterization of NPs and nanostructured films.

Transmission electron microscopy (TEM) and STEM-EDS. The samples were prepared by dropping V_2O_3 aqueous solution directly onto a carbon-coated TEM copper grid (400 mesh) followed by drying in air. TEM and STEM-EDS tests were carried out on TFS Talos F200X G2 transmission electron microscope with an acceleration voltage of 100 kV. High-resolution transmission electron microscopy (HRTEM) images were obtained on JEOL3100 microscope.

Scanning electron microscope (SEM) studies were carried out on TFS Nova 200 with an accelerating voltage of 1.5 kV.

X-ray photoelectron spectra (XPS) were obtained on a Kratos Analytical Axis Ultra apparatus. Powders of V_2O_3 NPs or chiral ITO films were placed on Cu tapes of bar. The working power set-up for these tests were 14 kV HT and 8 mA emission, and all tests were done at room temperature.

X-ray diffraction patterns (XRD) were acquired on a Rigaku Ultima-4 diffractometer using a continuous scanning mode with a scan step of 0.02 and a scan rate of 10 s per step.

Raman spectra were recorded on a laser micro Raman spectrometer (Invia, Renishaw) with a 532 nm wavelength laser.

Fourier Transform Infrared Spectroscopy (FTIR) were obtained on a bench-top Nicolet IS50 instrument using powders.

Vibrational circular dichroism (VCD). VCD measurements were performed on particles dispersed in heavy water (D_2O) at 33 mg/mL concentration using JASCO FVS-6000. A 100 µL drop was sandwiched between two BaF_2 crystals separated by a 50 µm Teflon spacer. A MCT-V detector was used to acquire IR and VCD data in the range 2000-850 cm^{-1} with a resolution of 4 cm^{-1} and a total of 100 and 500 accumulations, respectively. The sandwiched dispersion between BaF_2 crystals was rotated along an axis coinciding with the direction of the beam at a constant speed to avoid settling of particles. Corresponding IR and VCD were plotted as A and $\frac{\Delta A}{A}$, respectively with exclusion of 1300 to 1100 cm^{-1} range that corresponds to strong absorption from D_2O.

Raman Optical Activity (ROA). ROA measurements were performed on BioTools ChiralRaman-2X instrument using a 30 mg/mL concentration of nanoparticles in water. A 100 uL solution was placed in the cell holder and illuminated with a 100 mW powered laser for 1.5435 s for LCP and RCP each. A total of 3000 scans were accumulated and intermediate data was acquired at intervals of 3 min to monitor the effect of external disturbances. Baseline for water was acquired under identical settings and subtracted from the acquired signal from nanoparticles.

CD measurements (JASCO J-1700). Quartz cuvettes with a 1 cm path length were used for all tests with NPs solutions. The CD signals of all chiral films were recorded by dipping film in $ZnSO_4$ electrolyte. All *g*-factors were calculated from absorbance data measured simultaneously with a Jasco J-1700 circular dichroism spectrometer.

Figures S1 to S31

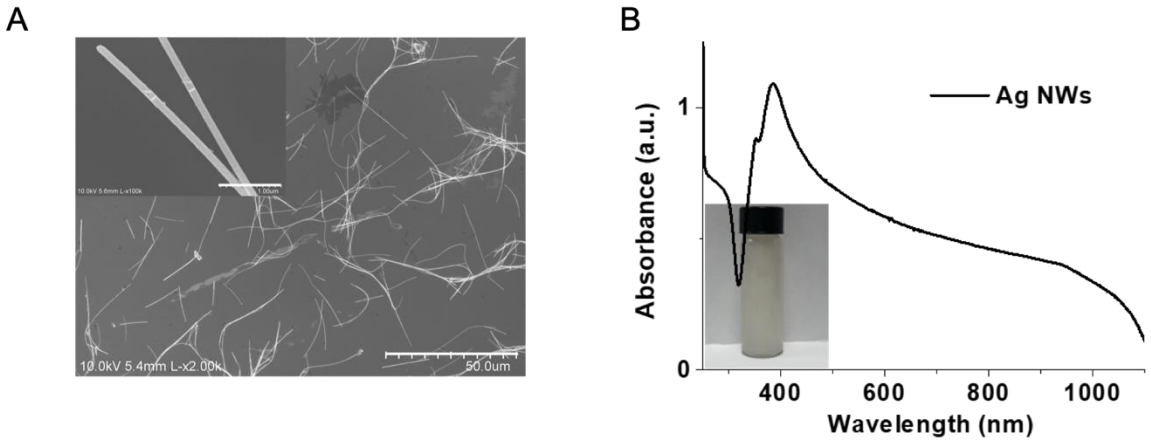

Figure S1. (A) SEM of Ag NWs (insert scale bar: 1 um). (B) Absorbance spectra of Ag NWs.

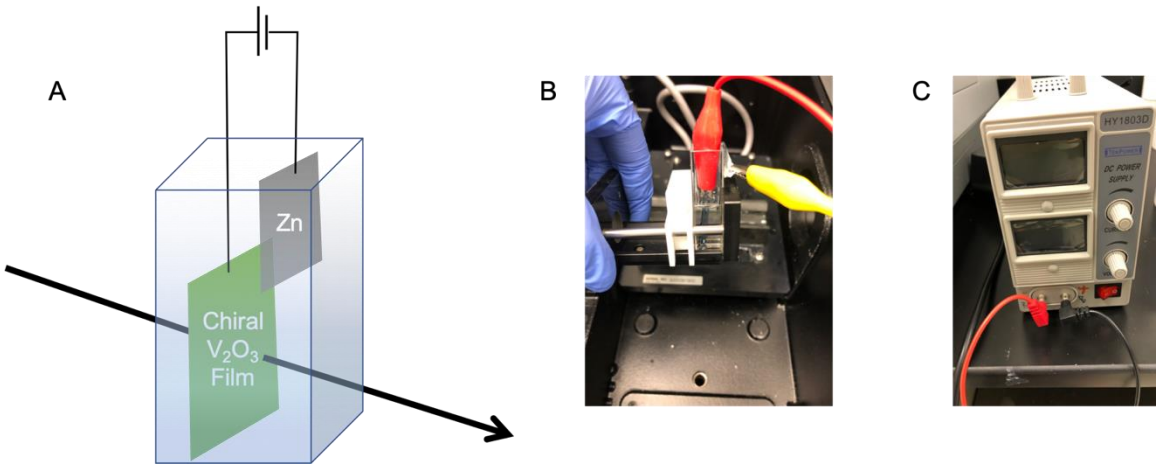

Figure S2. Set-up of in-situ CD measurements under cyclic voltage bias. (A) Schematic of the reaction setup for intercalation and deintercalation of Zn ions, (B) the corresponding actual reaction setup, including quartz cell, two electrodes (Zn foil and *L*-Film), (C) power supply.

Table S1. Electrical conductivity of metal oxides.

Category	**Resistivity (Ω·cm)**	**Ref.**
Mn_xO_y	5-8	55
Fe_xO_y	$4x10^{-3}$-0.25	56
ZnO	$7.5*10^3$	57
Co_3O_4	10^3-10^4	58
V_2O_3	**10^{-3}-10**	59,60

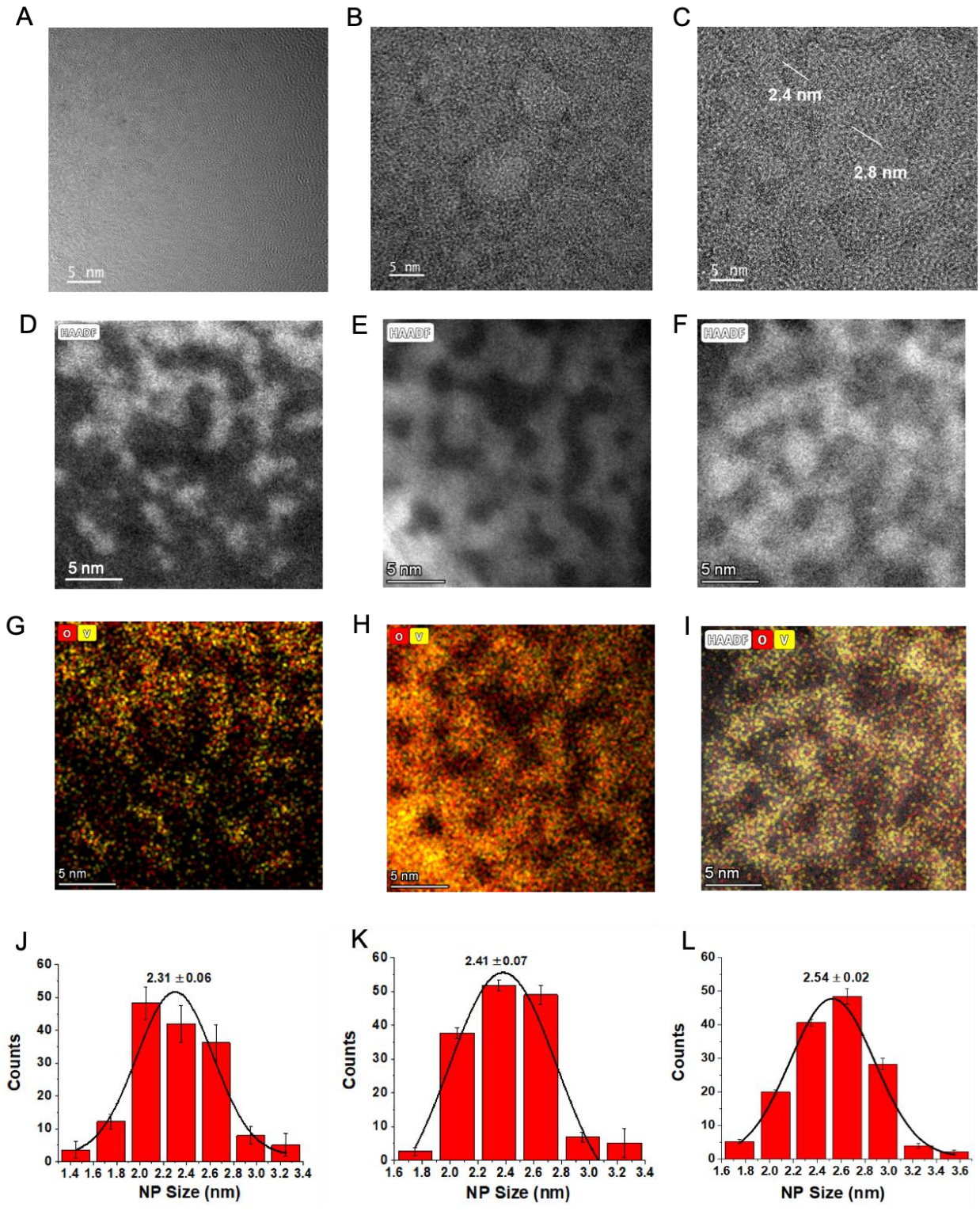
A
B
C
2.4 nm
2.8 nm
5 nm
D
E
F
HAADF
5 nm
G
H
I
O
V
HAADF O V
J
K
L
2.31 ±0.06
2.41 ±0.07
2.54 ±0.02
Counts
NP Size (nm)

Figure S3. HRTEM images of *L*-NPs for (A) pH 3, (B) pH 7, (C) pH 11. STEM and EDS of *L*-NPs (D and G) for pH 3, (E and H) pH 7, (F and I) pH 11. Size distributions of *L*-NPs for (J) pH 3, (K) pH 7, (L) pH 11.

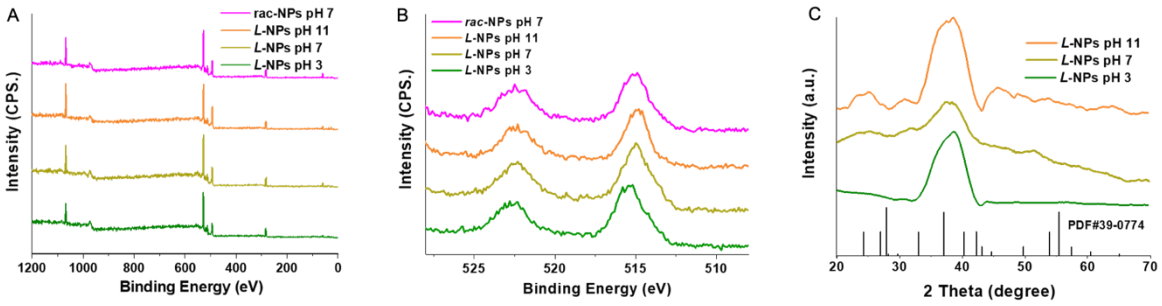

Figure S4. (A) Survey XPS spectra and (B) vanadium 2*p* region XPS spectra of *L*, *rac*-NPs. (C) XRD spectra of *L*-NPs at different pH values.

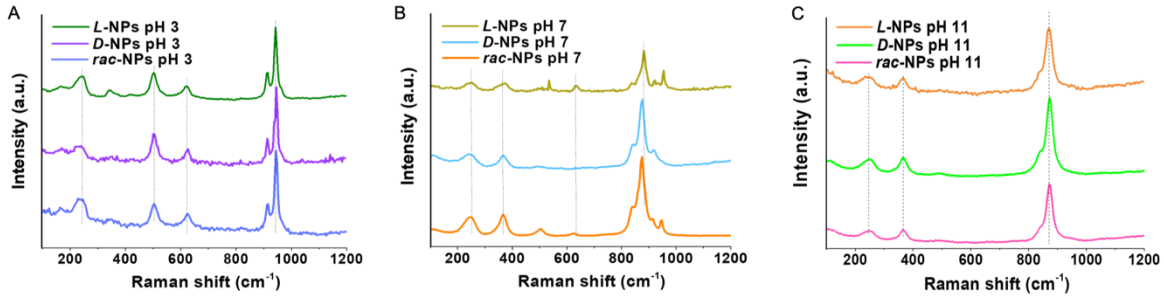

Figure S5. Raman spectra of *L*-, *D*- and *rac*-NPs at pH 3, 7, 11.

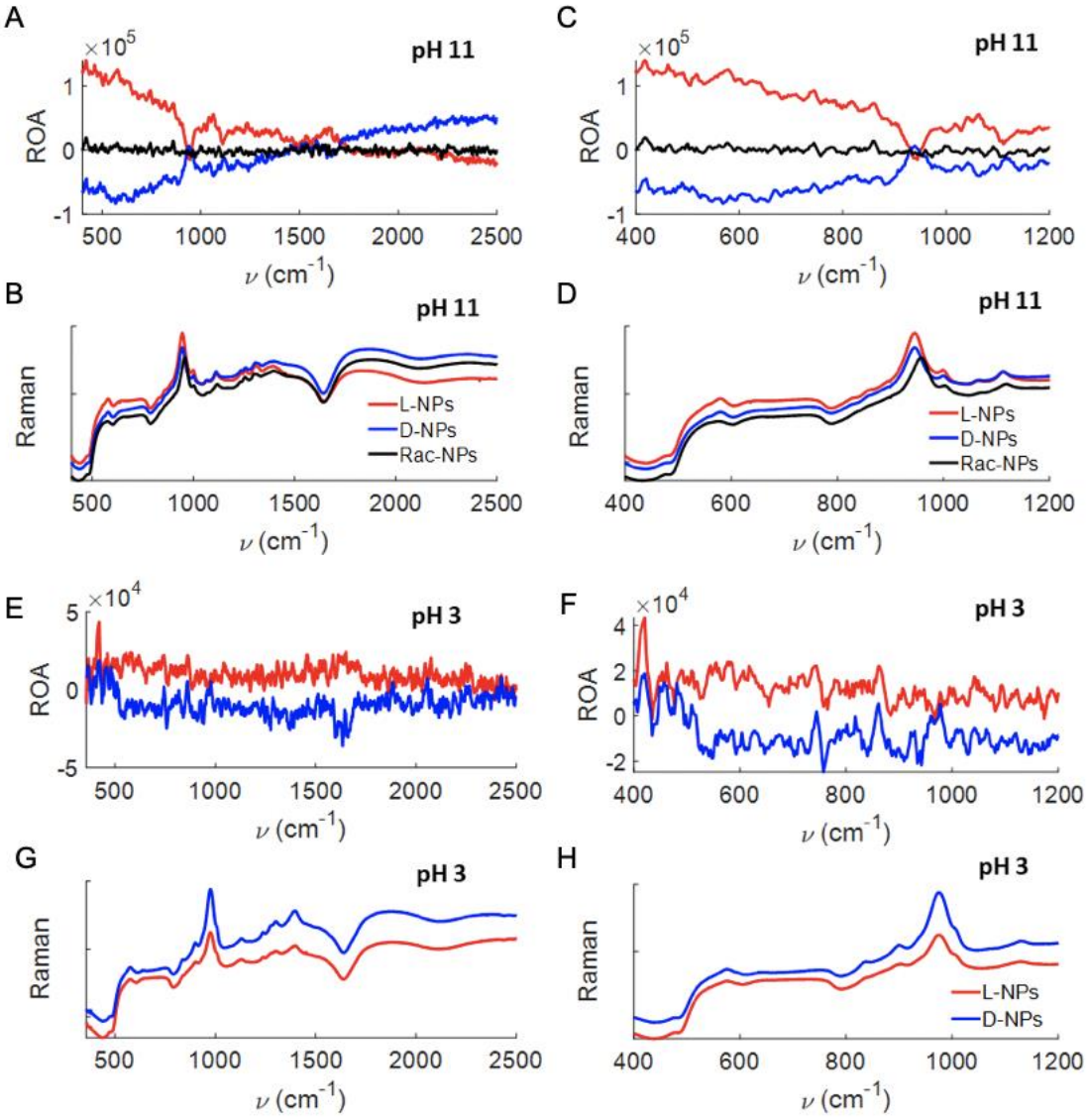

Figure S6. Raman scattering and Raman optical activity. Raman optical activity and the corresponding Raman spectrum plotted for nanoparticles at (A, B) pH 11 and (E, F), pH 3 in a wavenumber range of 400-2500 cm^{-1}. The 400-1200 cm^{-1} band of interest in the ROA and Raman spectrum is plotted for (C, D) pH 11 and (G, H) pH 3 nanoparticles. The peak for L-NPs at pH 11 is at 947 cm^{-1} and for L-NPs at pH 3 is at 972 cm^{-1}. The spectral red shift from pH 11 to

pH 3 is consistent with the acquired signal from FTIR. Particles at pH 11 show stronger mirror asymmetric bands in ROA spectrum below 600 cm^{-1} as compared to particles at pH 3, thereby suggesting stronger chiral vibrations of the nanoparticle cores.

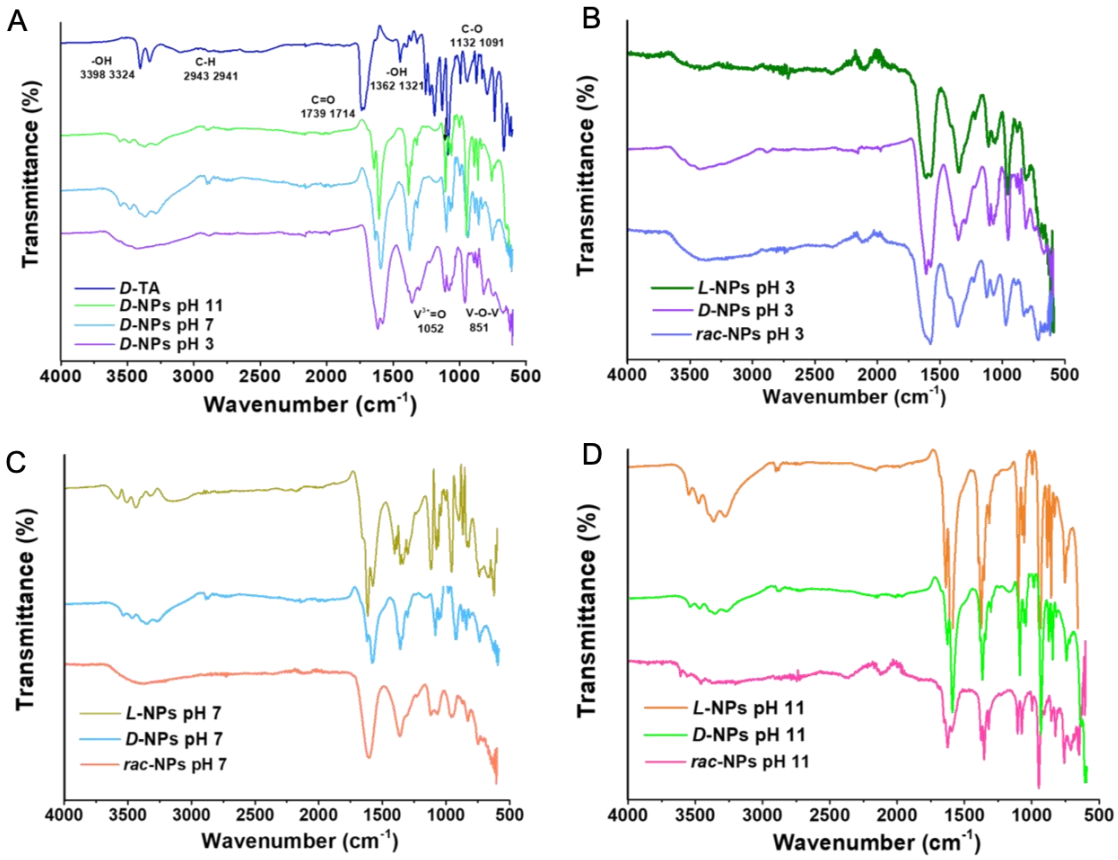

Figure S7. FTIR spectra of *L*-, *D*- and *rac*-NPs with pH 3, 7, 11.

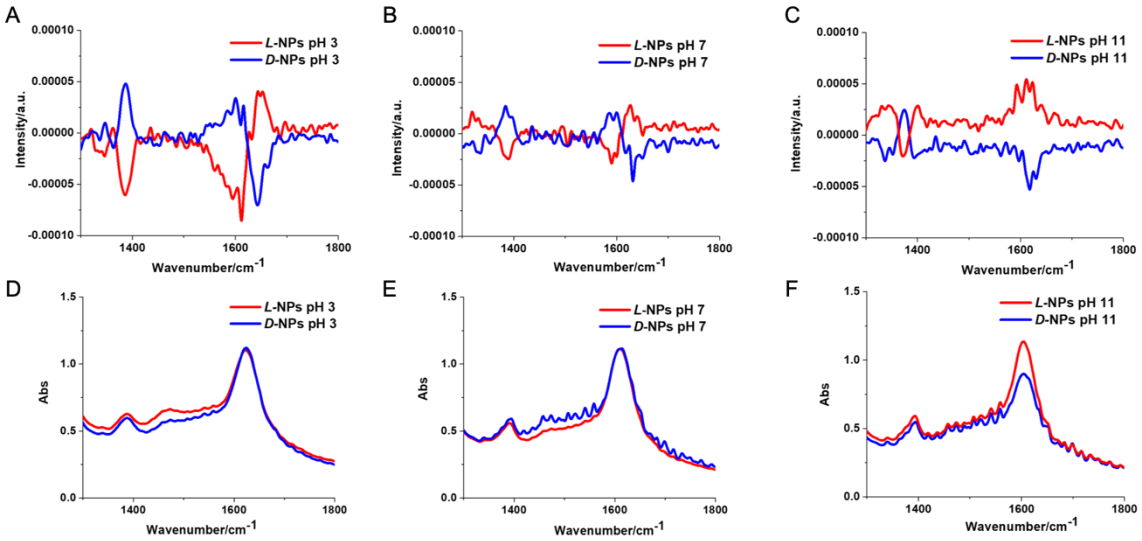

Figure S8. (A-C) VCD spectra and (D-F) FTIR spectra of *L*- and *D*-NPs at pH 3, 7, 11. A characteristic modulation of the amide II band centered at 1600 cm^{-1} suggests that the molecular bonding of TA changes significantly with pH as observed from MD simulations.

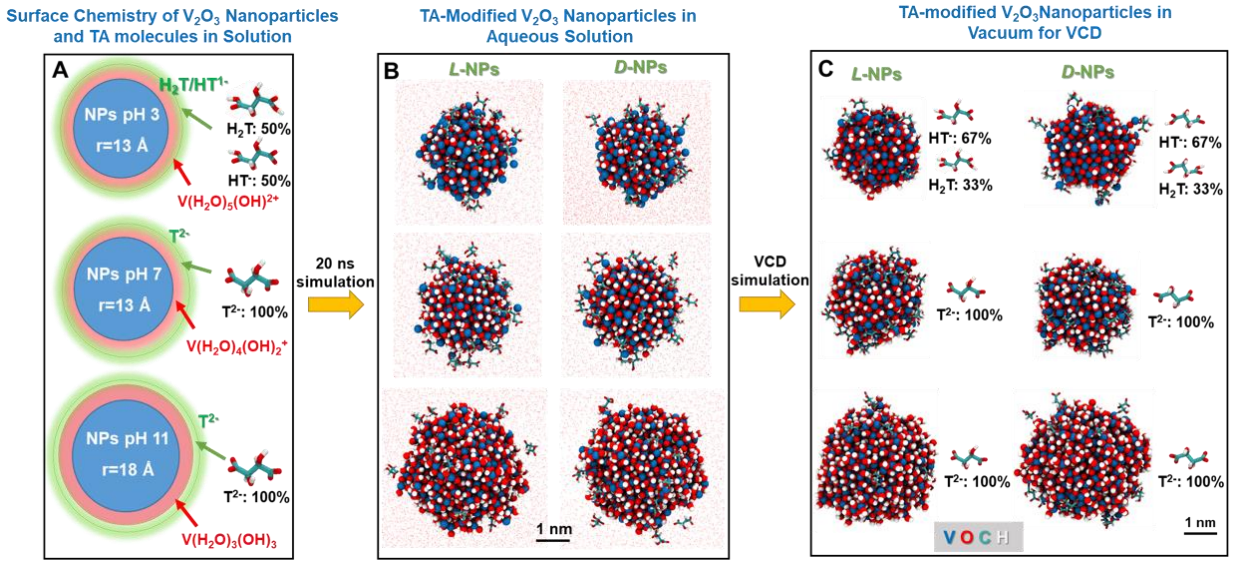

Figure S9. **Schematic of the atomistic models and simulation workflow.** (A) Details of the surface chemistry of V_2O_3 NPs and of the protonation state of TA molecules in solution at pH values of 3, 7, and 11. (B) Equilibrium structures of TA-modified V_2O_3 NPs in aqueous solution at pH values of 3, 7, and 11. (C) Equilibrium structures of TA-modified V_2O_3 NPs in vacuum for simulations of VCD spectra at pH values of 3, 7, and 11. The MD simulations show that the TA-modified NPs are stable in water (B). At a pH value of 3, although the initial ratio of H_2T:HT^- species was 50%:50%, the equilibrium structures show that TA species adsorbed on the NPs exhibit a ratio of 33%:67% (H_2T:HT^-). This difference demonstrates that the single deprotonated HT^- had higher affinity to the NPs surface compared to the pristine uncharged H_2T. At pH 7 and 11, T^{2-} was the dominant form of TA.

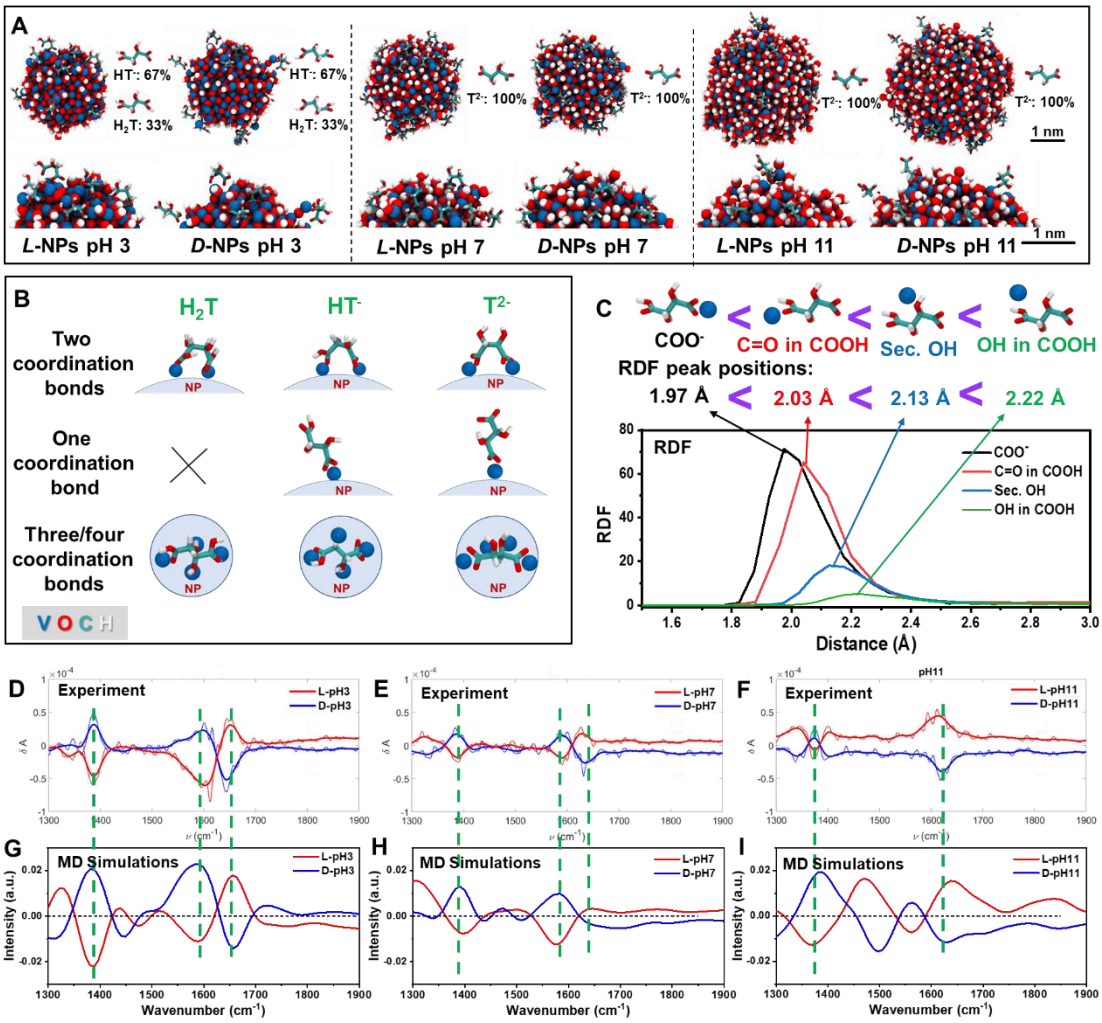

Figure S10. Models of the equilibrated V_2O_3 NPs in contact with TA, binding orientations, and VCD spectra from measurement and MD simulations. (A) The atomically resolved models of equilibrium structures and close-up views of the particle surfaces as utilized for the simulation of VCD spectra at pH values of 3, 7, and 11. The varying density of surface hydroxide ions and resulting binding patterns of TA species can be seen. (B) The typical binding conformations and number of coordination bonds of the TA species (H_2T, HT^-, and T^{2-}) on V_2O_3 NPs. (C) The radial distribution functions (RDF) between the O-groups of TA molecules and the

neighboring V atoms on the NPs surfaces for *L*-NPs pH 3. The corresponding first peak positions (*r*) indicate the closest coordinated V−O distance along with the schematic diagram of binding conformations. The RDF plots manifest COO^- groups possessed the shortest V−O distance (*r* = 1.97 Å), followed by C=O in terminal COOH (*r* = 2.03 Å), the secondary OH (*r* = 2.13 Å), and finally the OH in terminal COOH (*r* = 2.22 Å). A closer V−O distance generally means a stronger coordination affinity between the TA and NPs. (D-F) The experimental VCD spectra of the V_2O_3 NPs modified with TA at pH values of 3, 7, and 11. (G-I) The simulated VCD spectra of the V_2O_3 NPs modified with TA at pH values of 3, 7, and 11. A high degree of agreement is seen, which confirms realistic choices of model structures and simulations of the dynamics with IFF-CHARMM MD.

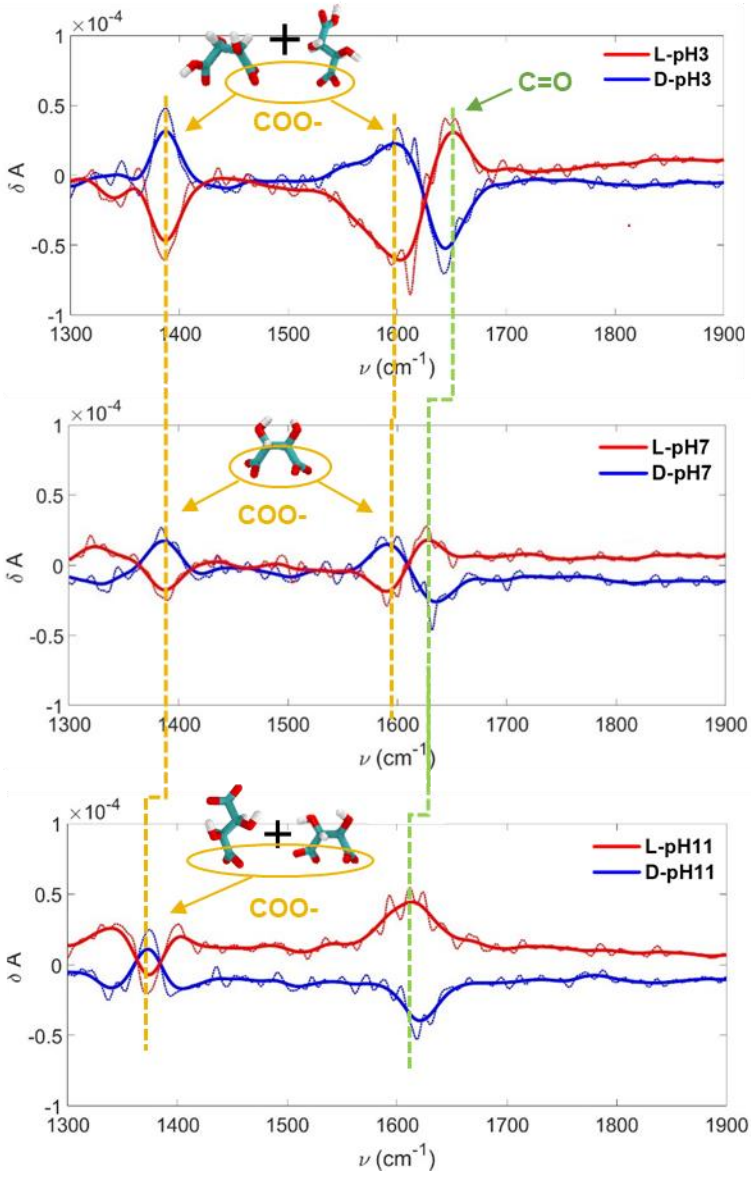

Figure S11. Comparison of the experimental VCD spectra of NPs pH 3, 7, 11 with marks of the peak shifts. The orange dashed line indicates the peaks from COO^-, while the green dashed line indicates the peaks from C=O. Herein, the symmetrical VCD peaks at around 1390 and 1590 cm^{-1} can be attributed to the stretching and asymmetric stretching vibrations of bonded COO^- groups, while the peak at around ~1640 cm^{-1} can be assigned to the C=O bond (consistent with FTIR

spectra in Fig. S7) [61,62]. For NPs pH 3, the peaks from bonded COO^- groups remained the same at around 1390 and 1590 cm^{-1}, while the C=O peak slightly blue shifted to 1660 cm^{-1} because COOH groups weakened coordination with NPs compared to COO^-. On the contrary, NPs pH 11 had a red shift of the peaks at 1380 cm^{-1}, arising from the increased single coordination bonds. Particularly, the peak at around 1590 cm^{-1} almost vanished for NPs pH 11 and the C=O peak further red shifted to around 1610 cm^{-1} due to the concurrent decrease of two coordination bonds and increase of single coordination bond.

Table S2. Copy of IFF parameters for all atoms during simulations. The energy expression corresponds to equation (1). The parameters for TA come from CHARMM36. r_{min} represents the distance of minimum energy between pairs of non-bonded atoms and epsilon the minimum energy in the Lennard-Jones term.

Nonbond parameters for all atoms	**Atomic charge (e)**	**r_{min} (Å)**	**Epsilon (kcal/mol)**	**Atomic mass (Da)**
V	1.5	2.08	0.2	50.9415
O	-1.0	3.44	0.2	15.9994
O in surface hydroxide	-0.9	3.5532	0.1553	15.9994
H in surface hydroxide	0.4	0.0002	0	1.00797
Zn^{2+} in $ZnSO_4$	1.7	2.022	0.005	65.3800
Zn^{2+} in V_2O_3	1.0	2.022	0.005	65.3800
S in SO_4^{2-}	0.5	4.2	0.3	32.0640
O in SO_4^{2-}	-0.55	3.1	0.22	15.9994
Bond parameters	**Bond length (Å)**	**Bond constant (kcal/mol/A^2)**		
surface hydroxide O−H	1.00	460		
S-O	1.505	380		
Angle parameters	**Angle (Å)**	**Angle constant (kcal/mol/rad^2)**		
O−S−O	109.5	170		

Table S3. The ratios of typical coordination bonding conformations of TA on NPs surface.

pH	NPs type	Number of coordination bonds		
		One	Two	Three/four
3	*L*	20%	70%	10%
	D	20%	70%	10%
7	*L*	0	90%	10%
	D	0	90%	10%
11	*L*	40%	40%	20%
	D	50%	40%	10%

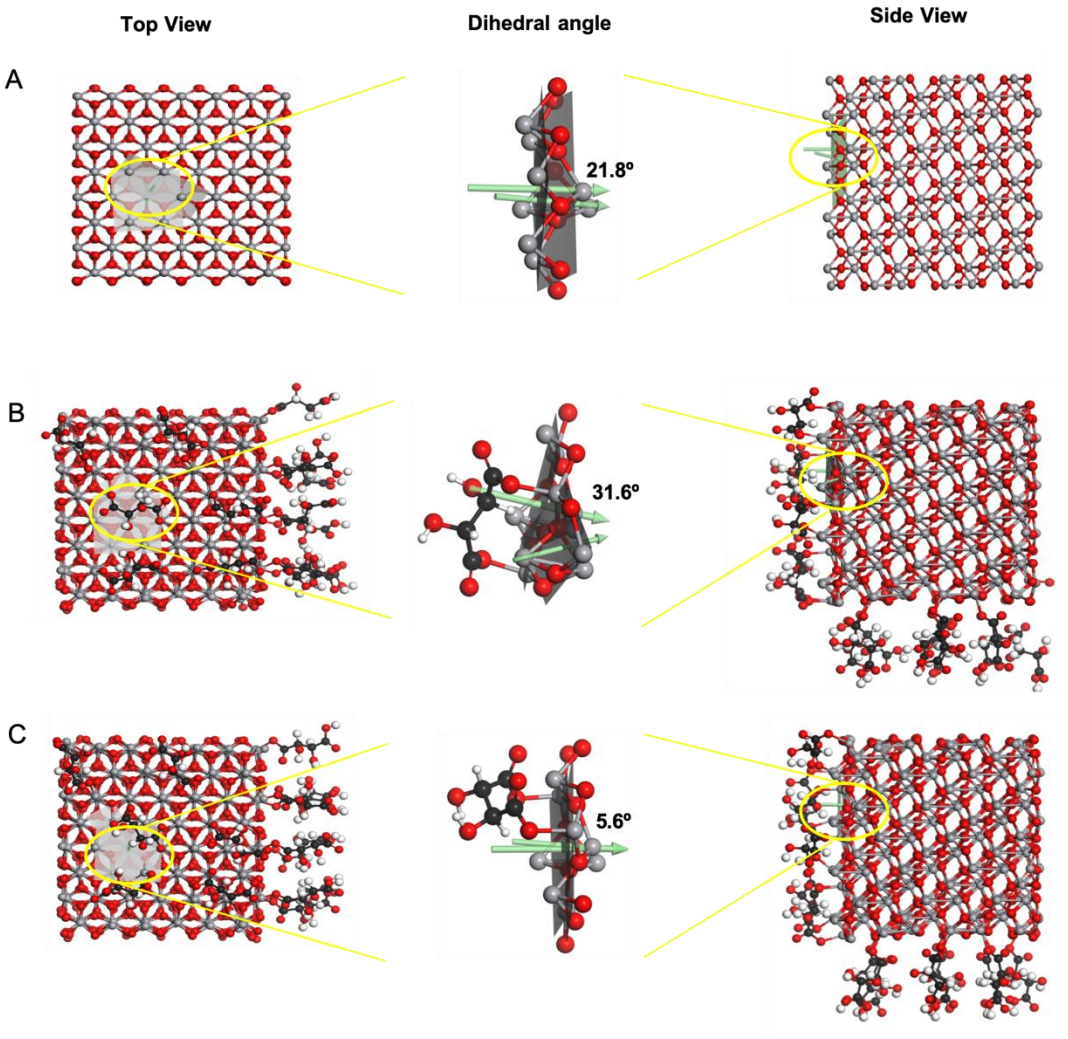

Figure S12. MD simulations of the atomic structure in the minimum energy state for (A) ligand-free, (B) *L*-, and (C) *D*-NPs. The COOH group of TA ligand bond to VO surface with bonding V−O. Each TA ligand has two COOH groups. One crystal plane of NP bond with one COOH, another plane of NP bond with two COOH groups. The MD simulations were performed with Forcite Plus module in Materials Studio. The Universal force field (UFF) was applied for bonded and unbonded interactions in the models.

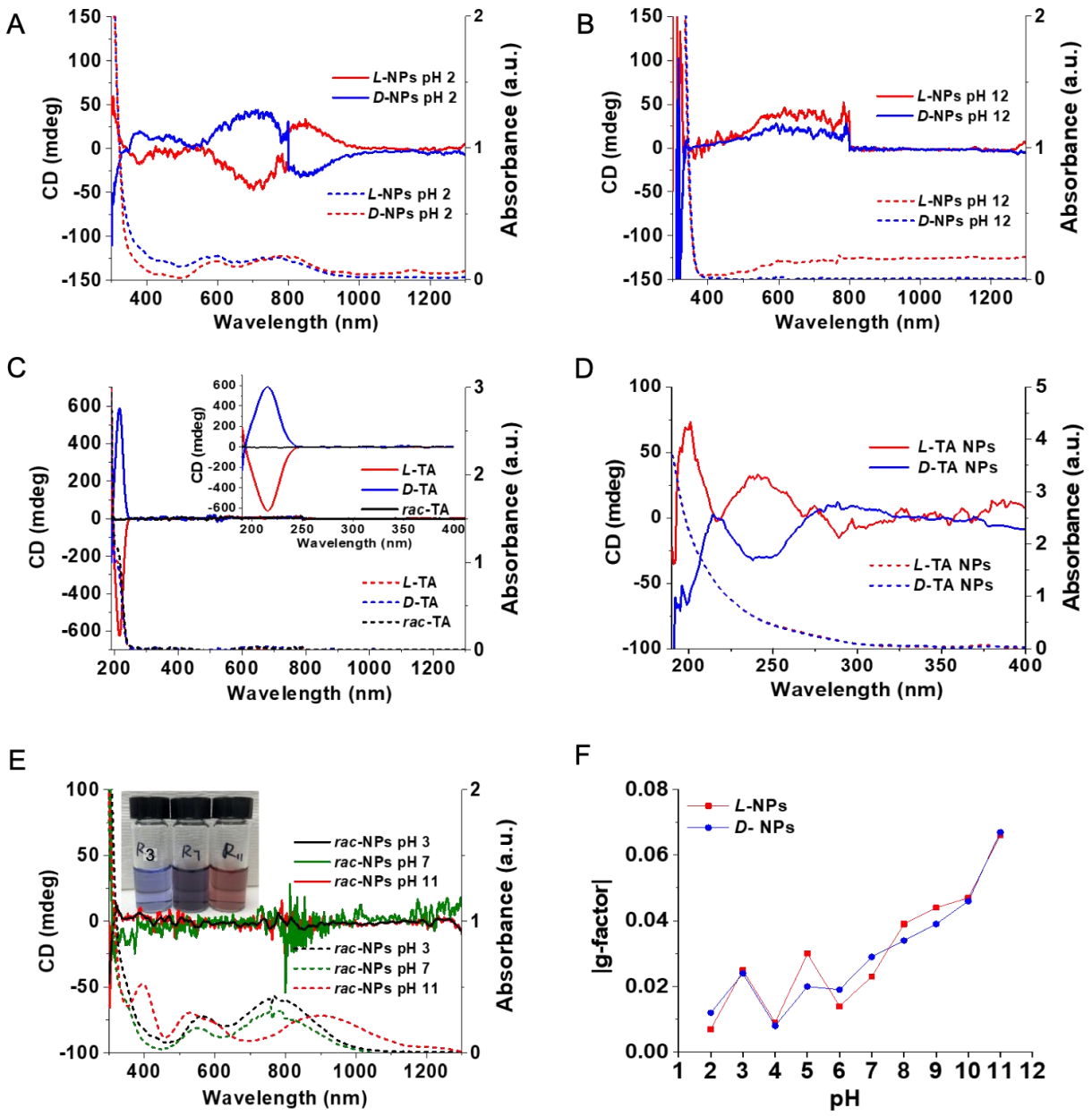

Figure S13. CD and absorbance spectra of *L*- and *D*- NPs with (A) pH 2, (B) pH 12, (C) *L/D/rac*-TA ligands, (D) CD spectra in the UV region of *L/D*-NPs, (E) *rac*-NPs (pH 3,7,11), (F) optical asymmetry *g*-factor spectra of *L/D*-NPs in NIR (pH 2-12).

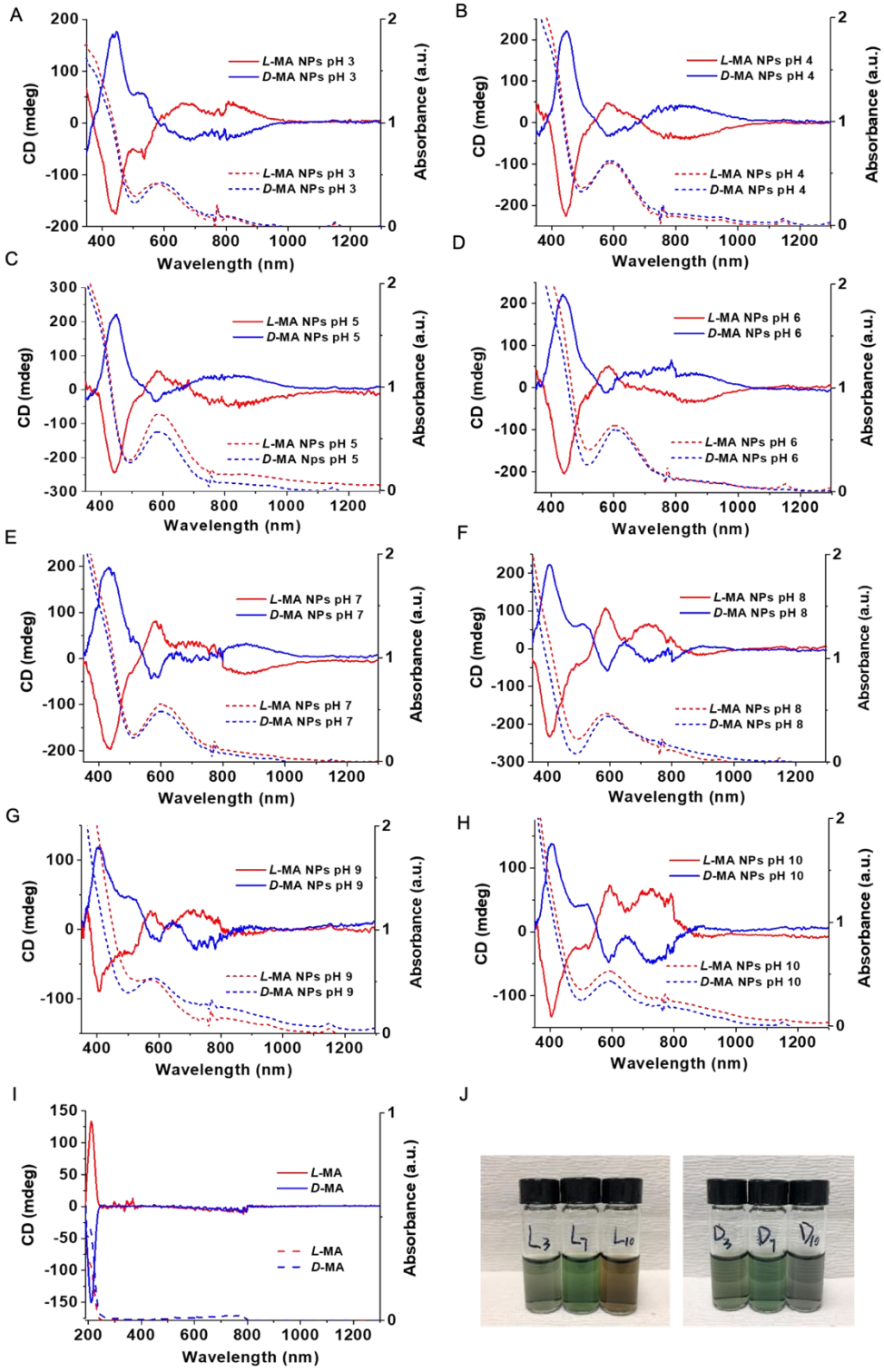
A
CD (mdeg)
Absorbance (a.u.)
Wavelength (nm)
L-MA NPs pH 3
D-MA NPs pH 3
B
L-MA NPs pH 4
D-MA NPs pH 4
C
L-MA NPs pH 5
D-MA NPs pH 5
D-MA Nps pH 5
D
L-MA NPs pH 6
D-MA NPs pH 6
E
L-MA NPs pH 7
D-MA NPs pH 7
F
L-MA NPs pH 8
D-MA NPs pH 8
G
L-MA NPs pH 9
D-MA NPs pH 9
H
L-MA NPs pH 10
D-MA NPs pH 10
I
L-MA
D-MA
J
L3
L7
L10
D3
D7
D10

Figure S14. CD and absorbance spectra of V_2O_3 NPs (A-H) with *L*- and *D*-MA, (I) *L*- and *D*-MA surface ligands. (J) Photographs of *L*- and *D*-MA V_2O_3 NPs dispersions.

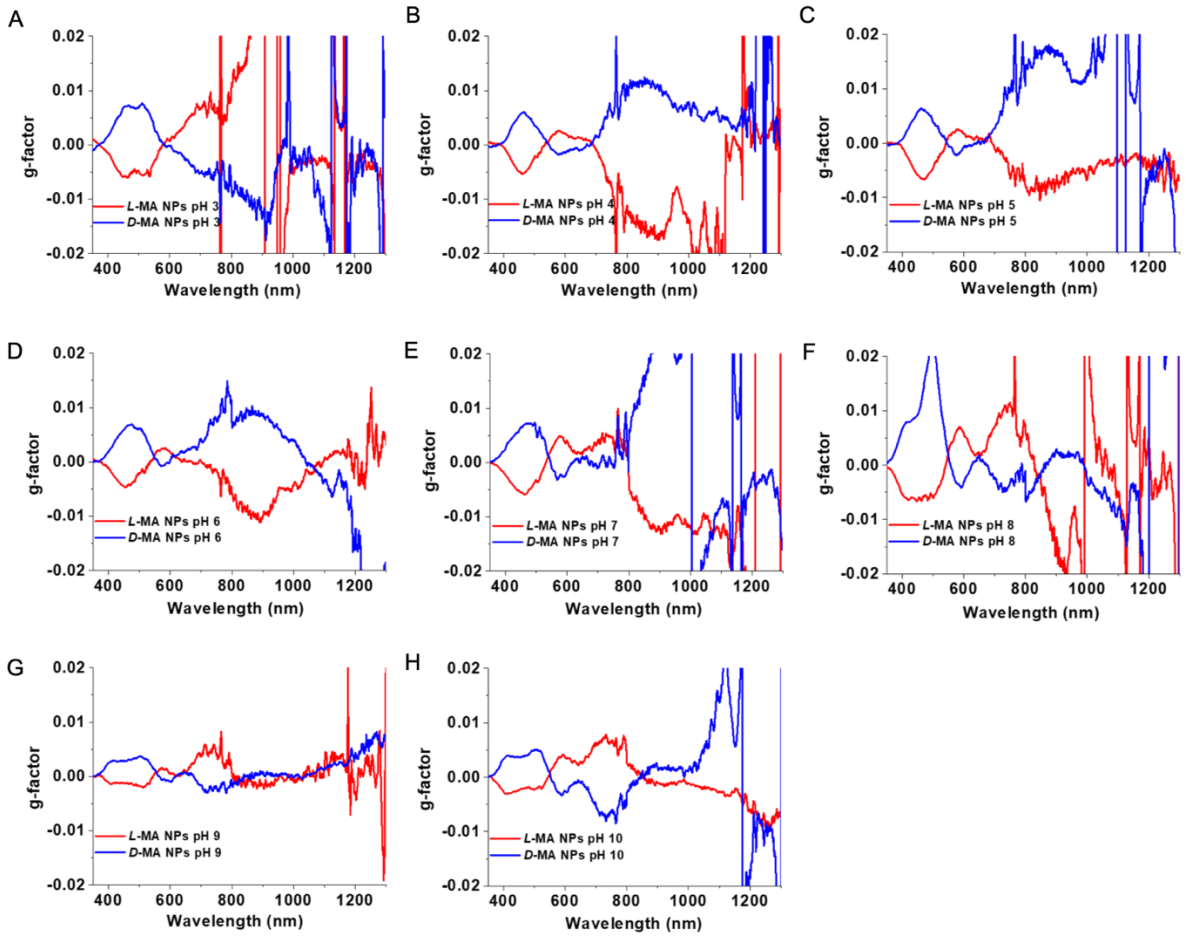

Figure S15. (A-H) Optical asymmetry *g*-factor spectra of *L*- and *D*-MA V_2O_3 NPs.

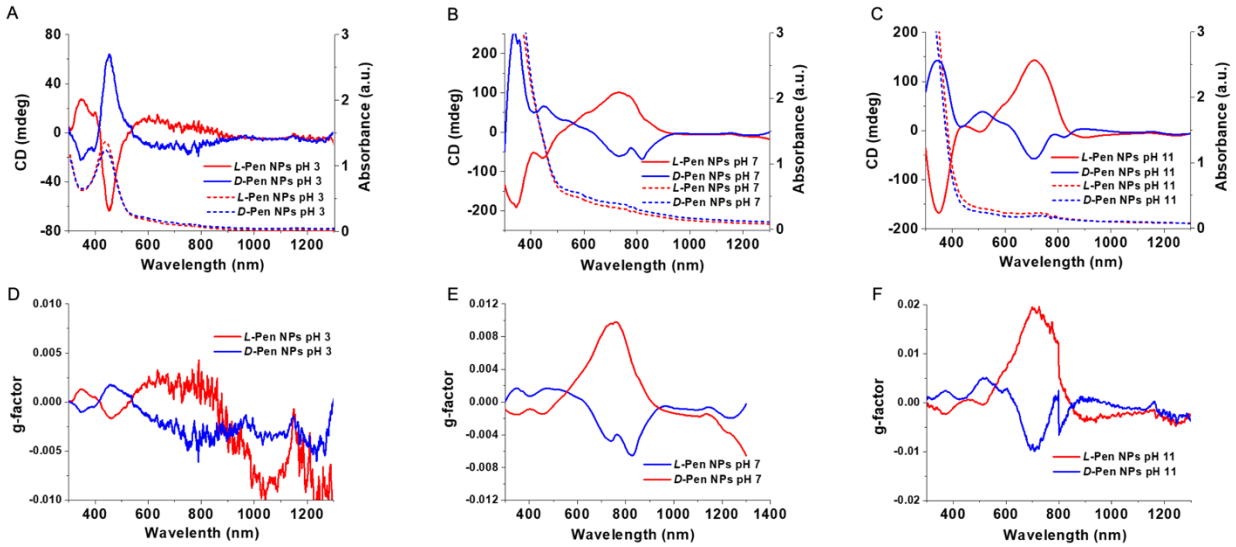

Figure S16. (A-C) CD and absorbance spectra of *L*- and *D*-Pen V_2O_3 NPs, (D-F) corresponding optical asymmetry *g*-factor spectra.

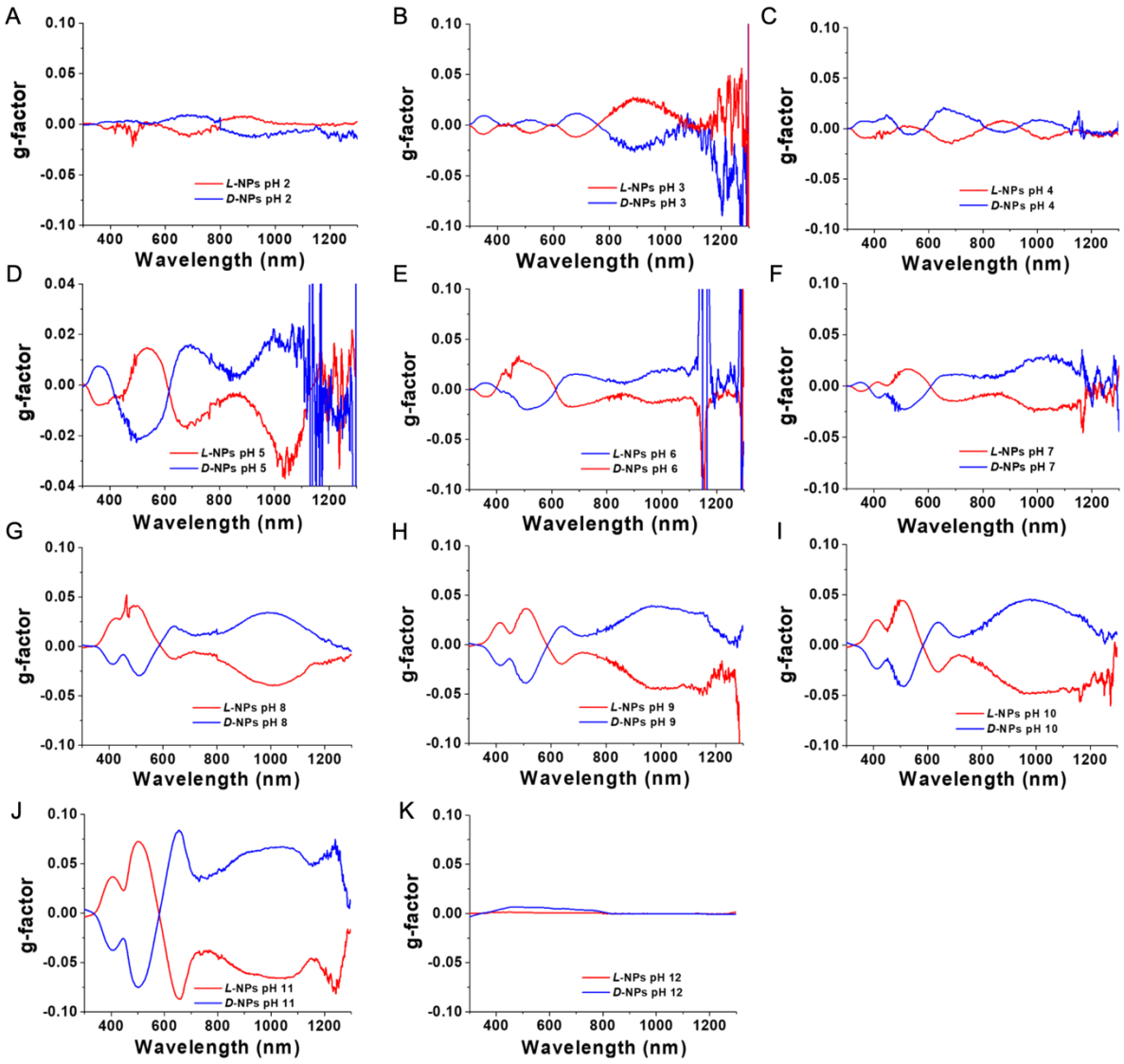

Figure S17. (A-K) Optical asymmetry *g*-factor spectra of *L*- and *D*-TA-NPs for pH from 2 to 12.

Table S4. Optical asymmetry *g*-factors of *L*- and *D*-TA V_2O_3 NPs (pH from 2 to 11) in aqueous dispersions.

pH	*L*-NPs λ_{CD}/nm	*g*-factors	*D*-NPs λ_{CD}/nm	*g*-factors
2	679	-0.010	691	0.008
3	898	0.025	900	-0.024
4	687	-0.015	662	0.020
5	532	0.016	507	-0.021
6	483	0.030	500	-0.020
7	1001	-0.023	1036	0.029
8	499	0.043	512	-0.029
9	975	-0.044	975	0.039
10	963	-0.047	981	0.046
11	654	-0.086	655	0.084

Table S5. Spectroscopic parameters of *L*- and *D*- NPs corresponding for NIR peaks for NPs synthesized at pH from 2 to 11.

pH	*L*-NPs λ_{CD}/nm	*g*-factors	*D*-NPs λ_{CD}/nm	*g*-factors
2	906	0.007	906	-0.012
3	898	0.025	900	-0.024
4	1031	-0.009	1020	0.008
5	1041	-0.030	1001	0.020
6	991	-0.014	986	0.019
7	1001	-0.023	1036	0.029
8	996	-0.039	998	0.034
9	975	-0.044	975	0.039
10	963	-0.047	981	0.046
11	1244	-0.079	1240	0.071

Table S6. Comparison of *g*-factors observed in chiral NPs and assemblies.

	Category	Material	Chiral ligand	Size (nm)	Wavelength range (nm)	Highest g-factor/wavelength (nm)	NIR g-factor/wavelength (nm)	Ref
NPs	Metal NPs	Au	*N*-isobutyryl-Cysteine	~NPs	200-600	0.001/475	0	[63]
		Ag	Cysteine	~2	200-400	0.005/400	0	[64]
		Cu	Cysteine	~2	200-400	0.001/325	0	[64]
	Semiconductor NPs	CdSe	Cysteine	~5	350-700	0.0002/575	0	[65]
		CdS	Penicillamine	~2	200-390	0.0005/250	0	[66]
	Ceramic NPs	Co_3O_4	Cysteine	~5	200-800	0.02/550	0	[2]
		WO_{3-x}	Aspartic acid	~2	400-1100	0.0018/560	0.0002/1050	[24]
		MoO	Cysteine	~3	500-900	0.007/580	0.0003/825	[67]
		V_2O_3	**Tartaric acid**	**~2**	**300-1300**	**0.086/655**	**0.079/1244**	**In this work**
Assemblies	Metal assemblies	Au helix	Tannic Acid	~30 micrometers	450-700	0.0001/600	0	[68]
		Au assembly	Guanosine		400-1300	0.0038/700	0.0068/1100	[9]
	Semiconductor assemblies	CdTe Helices	Cysteine	~2000	300-1300	0.06/1150	0.06/1150	[27]
	Ceramic	Cobalt oxide	Cysteine	~60	200-800	0.018/280	0	[69]

assemblies	supraparticles

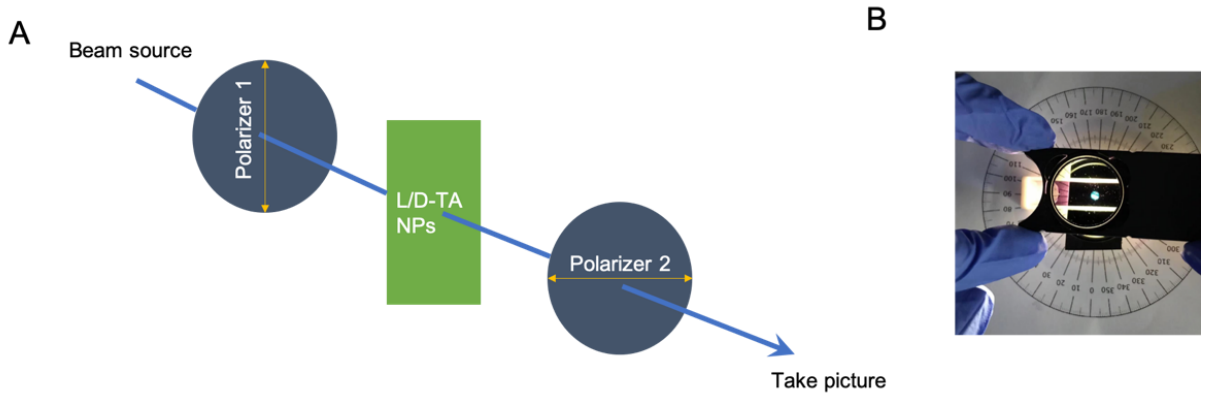

Figure S18. (A and B) rotation experimental set up for visible-NIR polarization rotation**.** (Visible light source: LED from iPhone's flashlight. NIR light source: HL-2000-LL light source with wavelength 360-2400 nm, camera: SenS SWIR 320V-ST/G-STE with 900-1700 nm.)

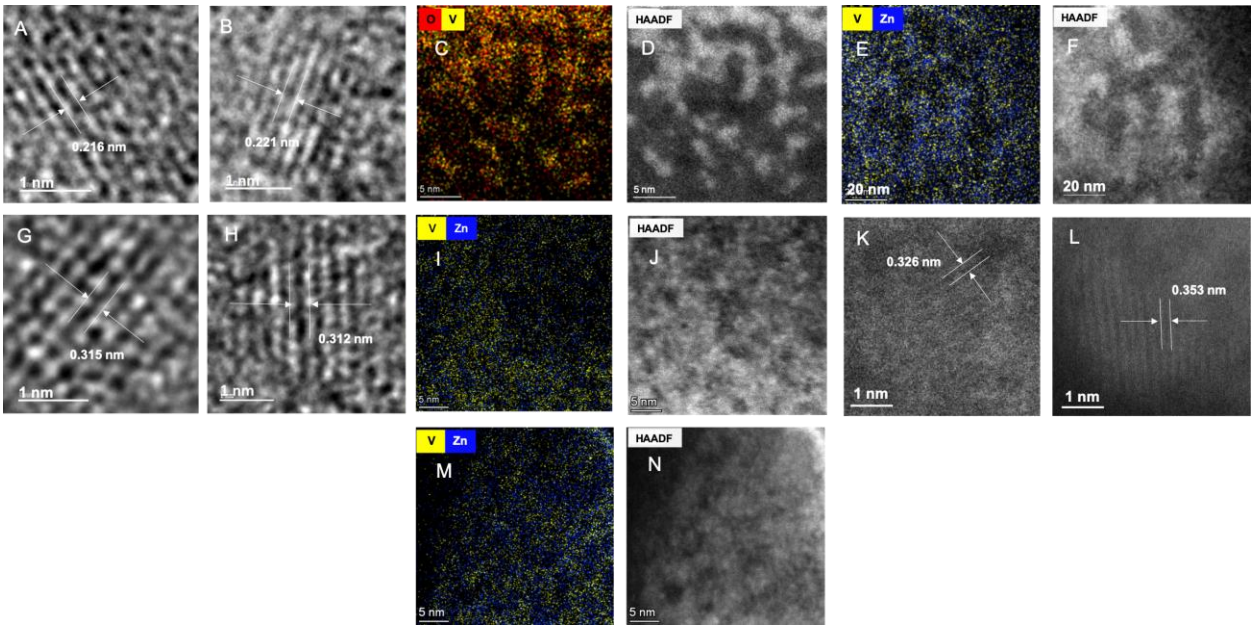

Figure S19. (A and B) HRTEM of *L*-NPs pH 3, (C and D) STEM-EDS of *L*-NPs pH 3, (E and F) STEM-EDS of Zn-intercalated *L*-NPs pH 3, (G and H) HRTEM of Zn-intercalated *L*-NPs pH 3, (I and J) STEM-EDS and (K) HRTEM of Zn-intercalated *L*-NPs pH 7, (L) HRTEM and (M and N) STEM-EDS of Zn-intercalated *L*-NPs pH 11.

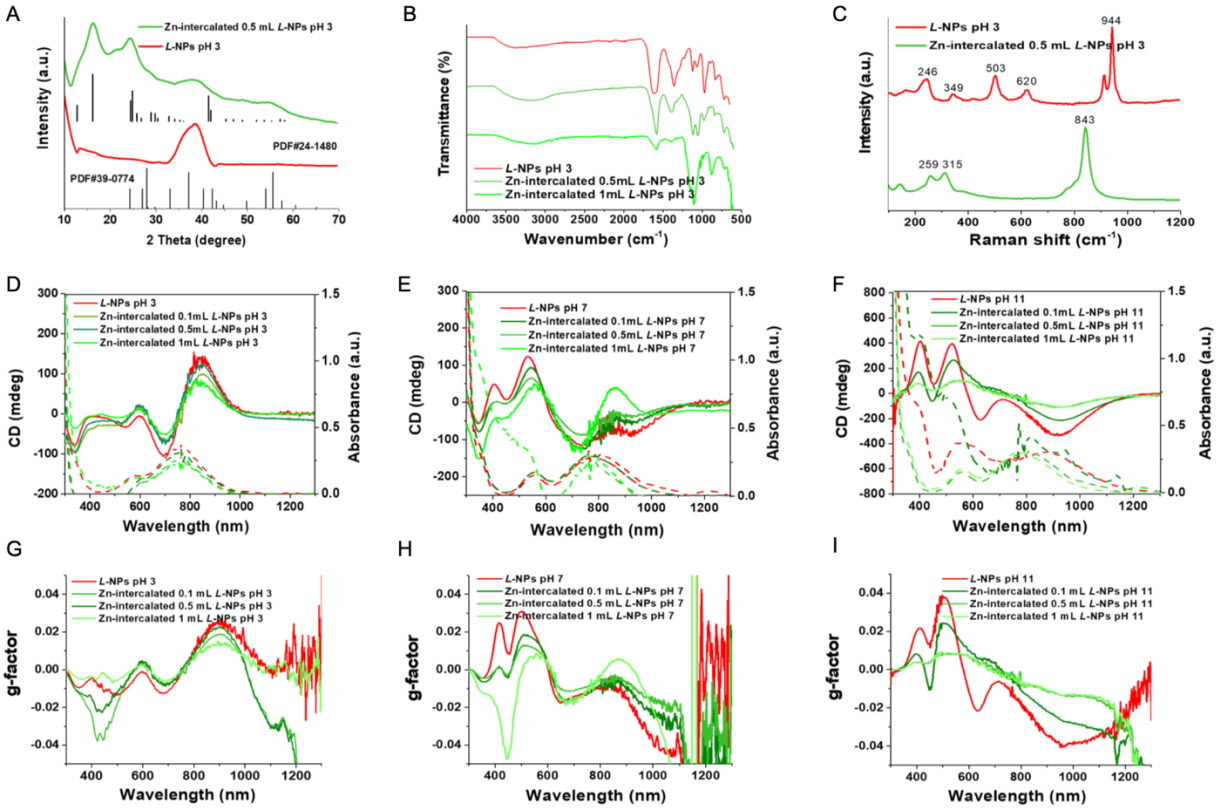

Figure S20. (A) XRD, (B) FTIR, (C) Raman spectra of *L*-NPs pH 3 and Zn-intercalated *L*-NPs pH 3. (D-F) CD and Absorption spectra of *L*-NPs at pH 3, 7 and 11 and different Zn-intercalated *L*-NPs at pH 3, 7 and 11, (G-I) corresponding optical asymmetry *g*-factor spectra.

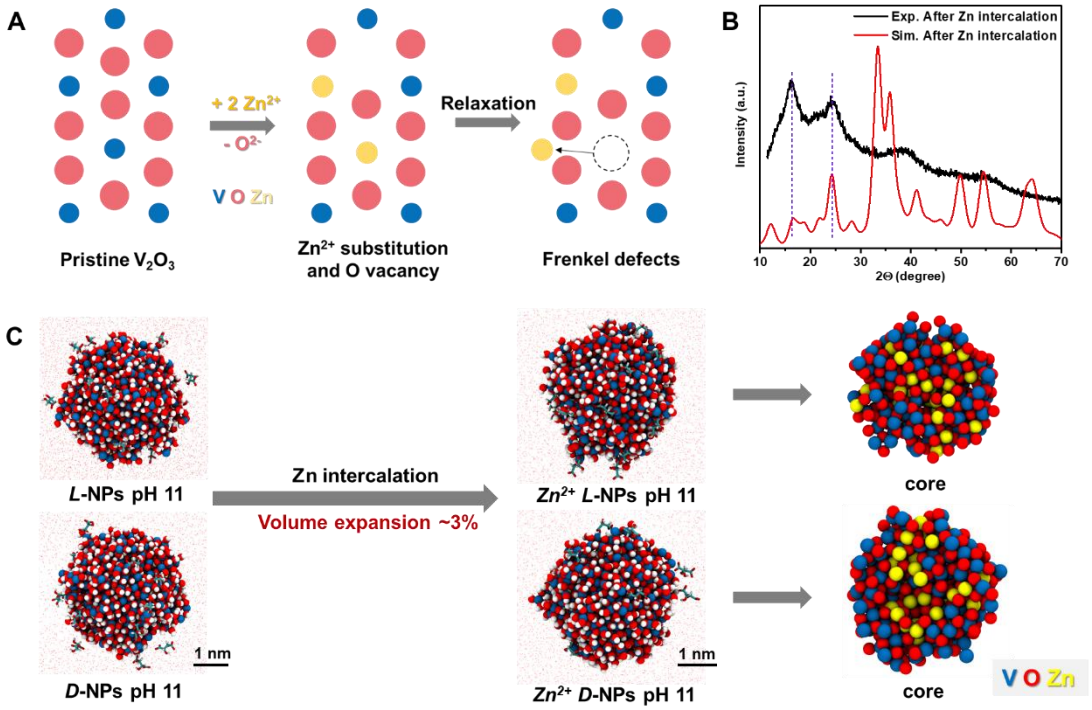

Figure S21. (A) Schematic of the evolution of the Zn^{2+} intercalated V_2O_3 structures and the formation of the Frenkel defects after relaxation, as seen in molecular dynamics simulation. (B) The comparison of the measured XRD pattern and the simulated diffraction pattern after Zn intercalation into V_2O_3 NPs at pH = 11. (C) The volume expansion of the NPs at pH = 11 induced by Zn^{2+} intercalation. The magnified core structures show the positions of the intercalated Zn^{2+} ions.

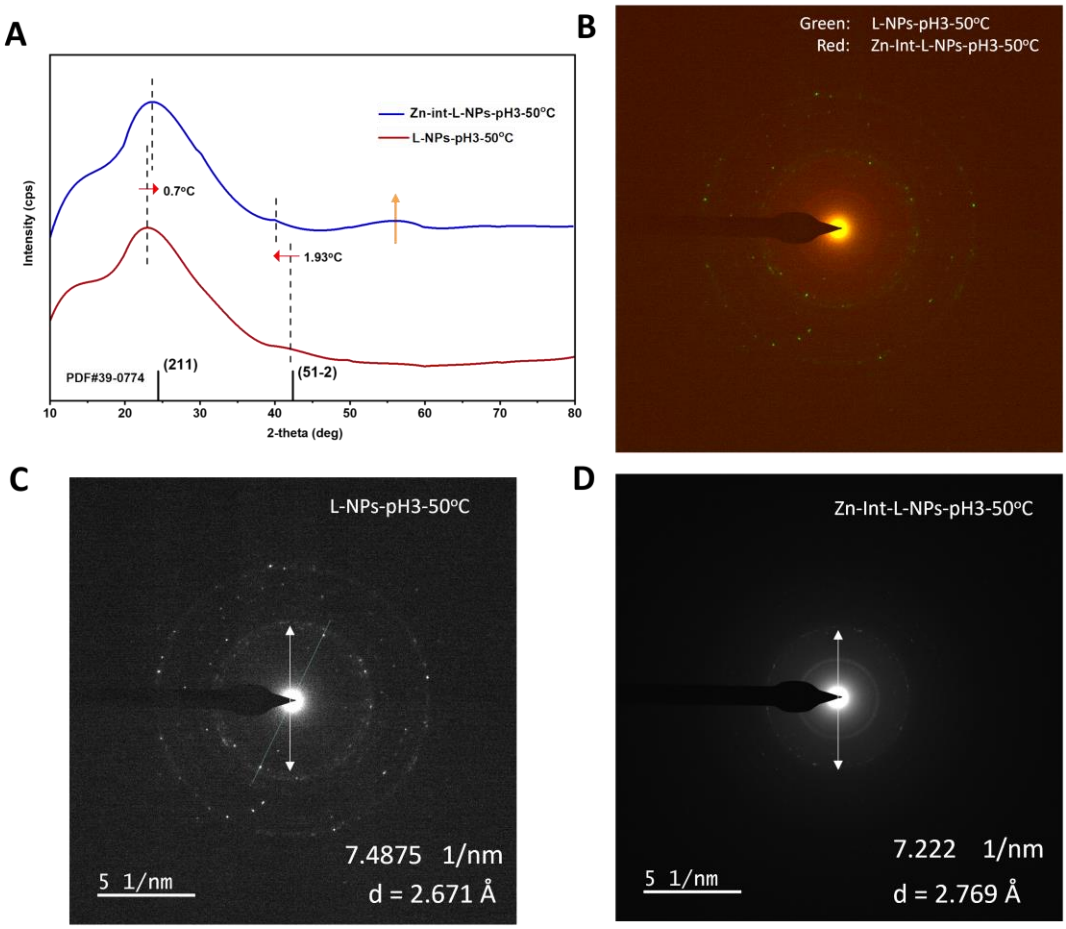

Figure S22. (A) XRD, and (B-D) Electron diffraction patterns of L-NPs before and after Zn-intercalation, the L-NPs were synthesized under 50^{o}C at pH3. (A) Compared with initial L-NPs-Ph3-50^{o}C, after Zn-intercalation the XRD diffraction of face (211) shows right shift, and face (51-2) has blue shift. New peak appeared around 2Theta=55^{o}, which is expected by the XRD simulation of L-NPs after Zn-intercalation. (B) Merge of two electron diffraction patterns from C and D. (C-D) Electron diffraction patterns with related lattice spacing of L-NPs at pH 3 before and after Zn-intercalation. Here peaks correspond to the diffraction of the [41-1] crystal planes of monoclinic V_2O_3 with standard lattice spacing 2.700Å.

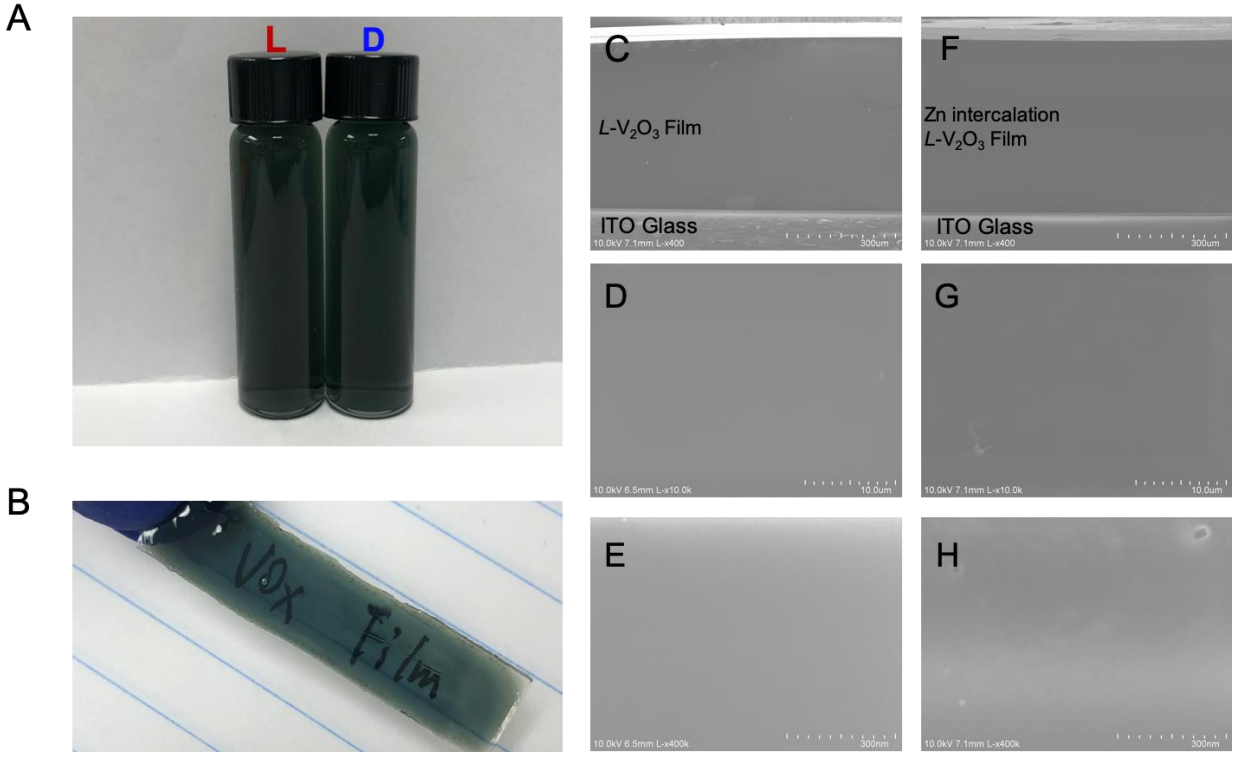

Figure S23. (A) Photograph of *L*- and *D*- NPs in H_2O, (B) *L*-V_2O_3 film. The film is transparent as can be seen by the writing behind it. SEM images of (C-E) the *L*-V_2O_3 film and (F-H) Zn ions intercalation of *L*-V_2O_3 film. (C and F) SEM images of cross-section view of the film and (D, E, G and H) SEM images of top-down view of the film surface.

.

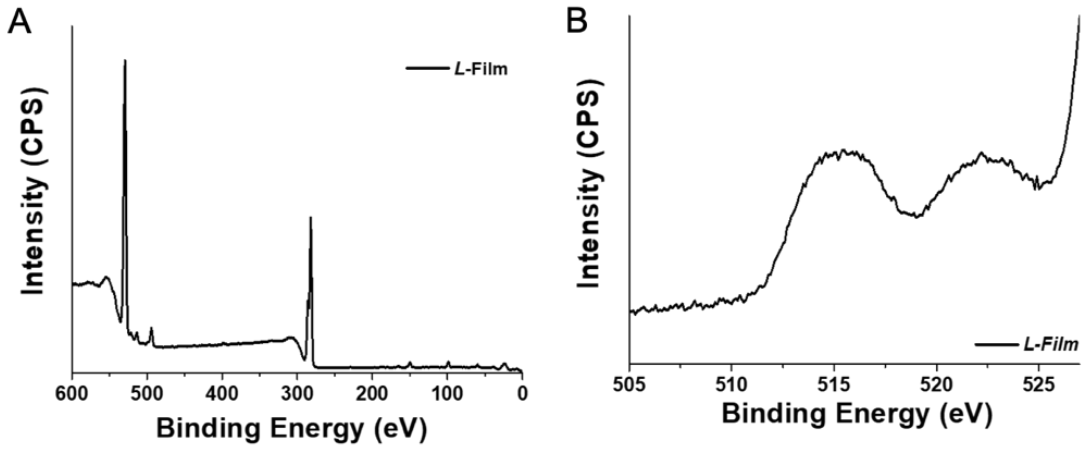

Figure S24. XPS of *L*-TA V_2O_3 LBL multilayer films.

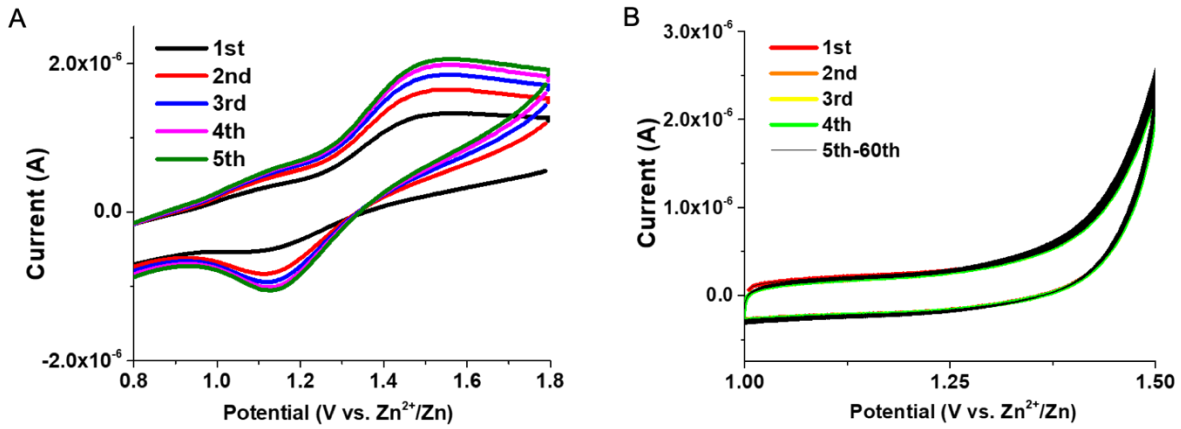

Figure S25. (A) Cyclic voltammetry (CV) curves of the *L*-TA-V_2O_3 composite film made only from NPs without CNTs or Ag NWs. (B) CV curves for 60 cycles run on *L*-TA-V_2O_3 film.

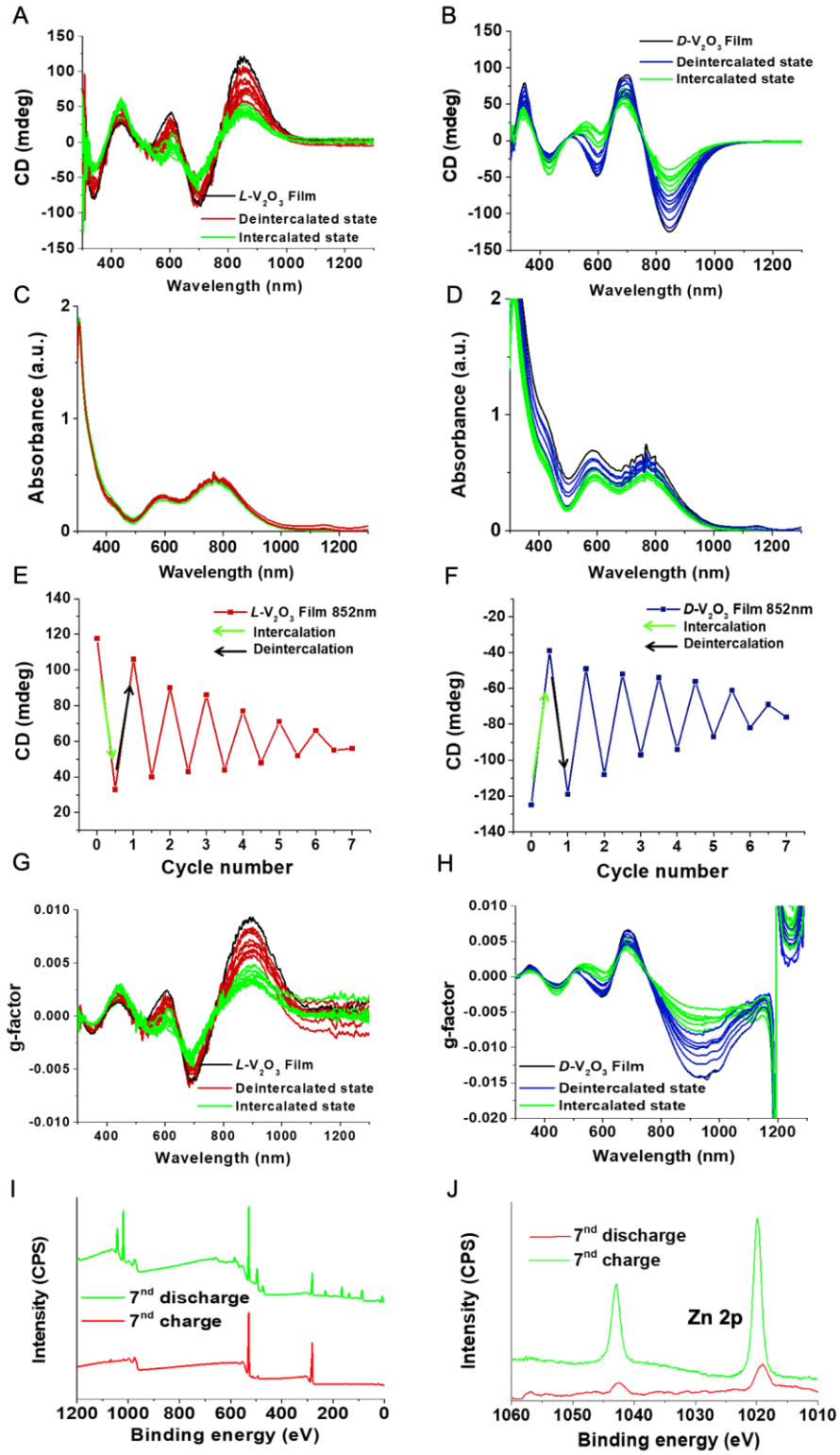

Figure S26. (A and B) CD and (C and D) absorbance of *L*-TA and *D*-TA V_2O_3 NP films, (E and

F) cycling performance of the films (CD intensity of films at 852 nm with zinc ions intercalation and deintercalation), (G and H) corresponding g-factor spectra, (I and J) XPS spectra of V_2O_3 film in the 7 cycle after intercalation and deintercalation.

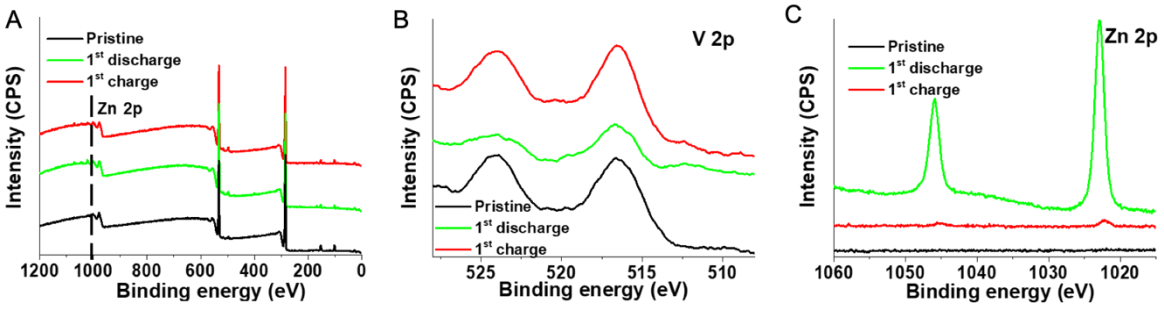

Figure S27. XPS spectra of V_2O_3 film in origin state, the first cycle after intercalation and deintercalation.

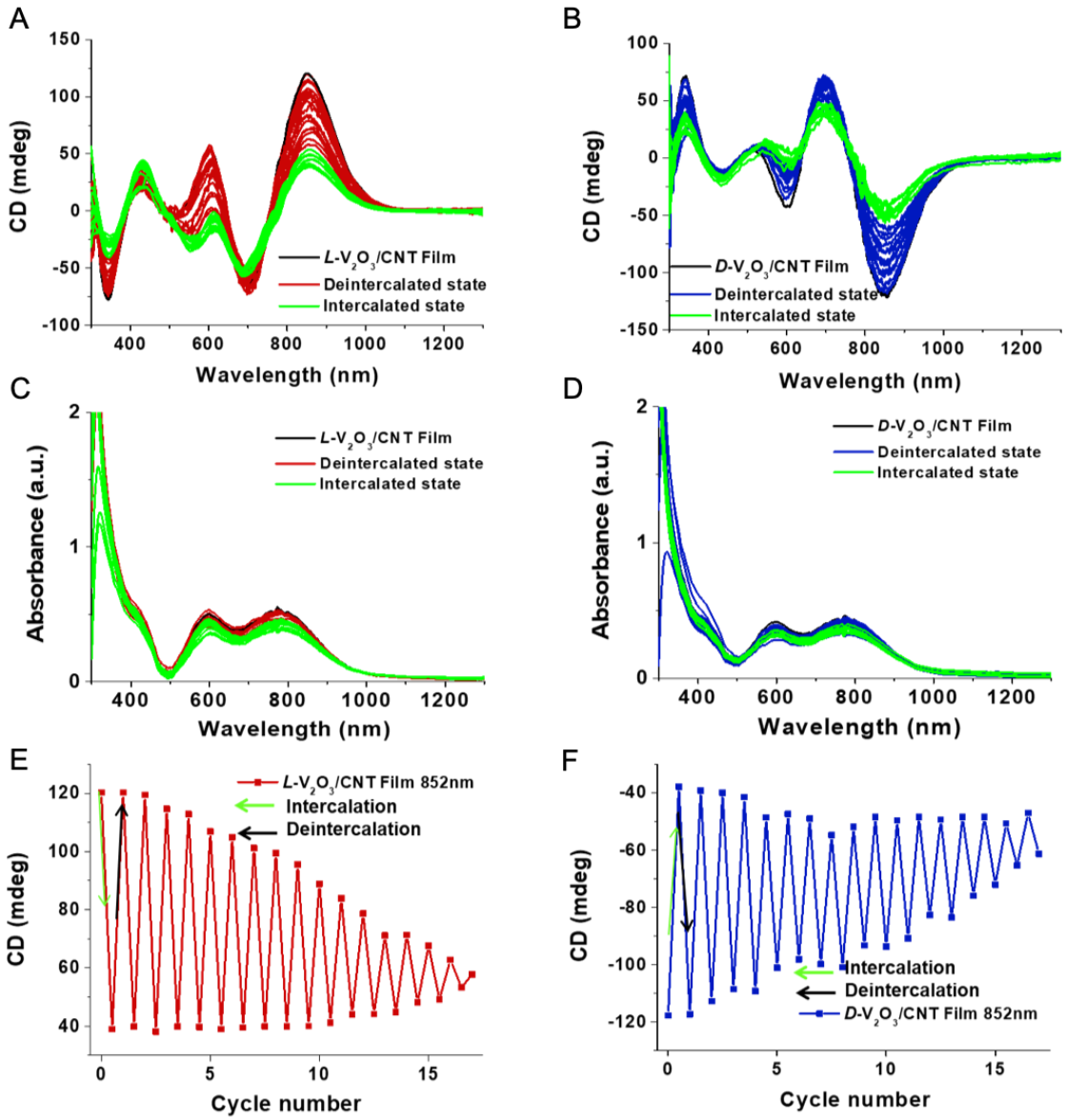

Figure S28. (A and B) CD and (C and D) absorbance spectra of *L*-TA and *D*-V_2O_3/CNT films, (E and F) cycling performance of the films (CD intensity of films at 852 nm with zinc ions intercalation and deintercalation).

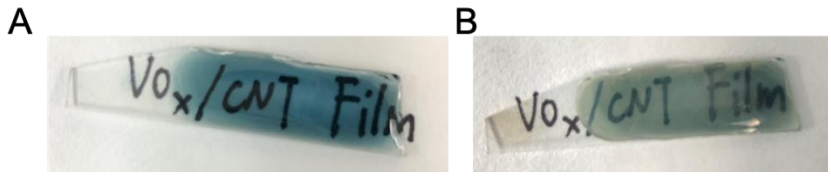

Figure S29. Photographs of *L*-V_2O_3/CNT film before (A) and after (B) 17 cycles.

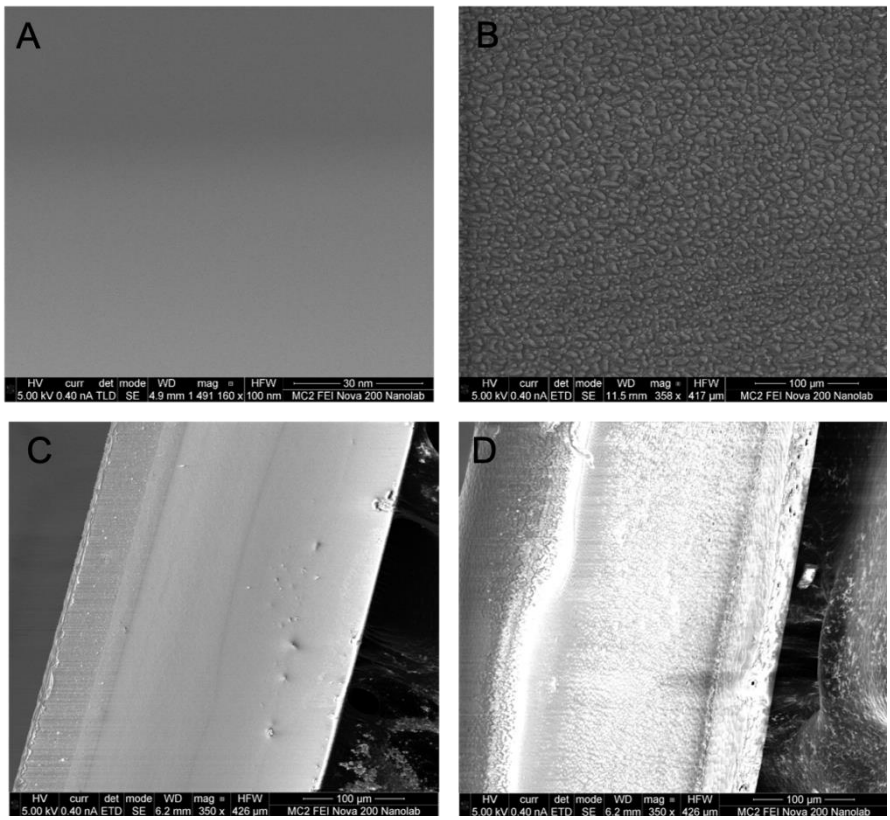

Figure S30. SEM images of the composite films obtained for deintercalated state. Top-down view of the *L*-V_2O_3/CNT film surface before (A) and after (B) 17 cycles, cross-section view of the *L*-V_2O_3/CNT film before (C) and after (D) 17 cycles.

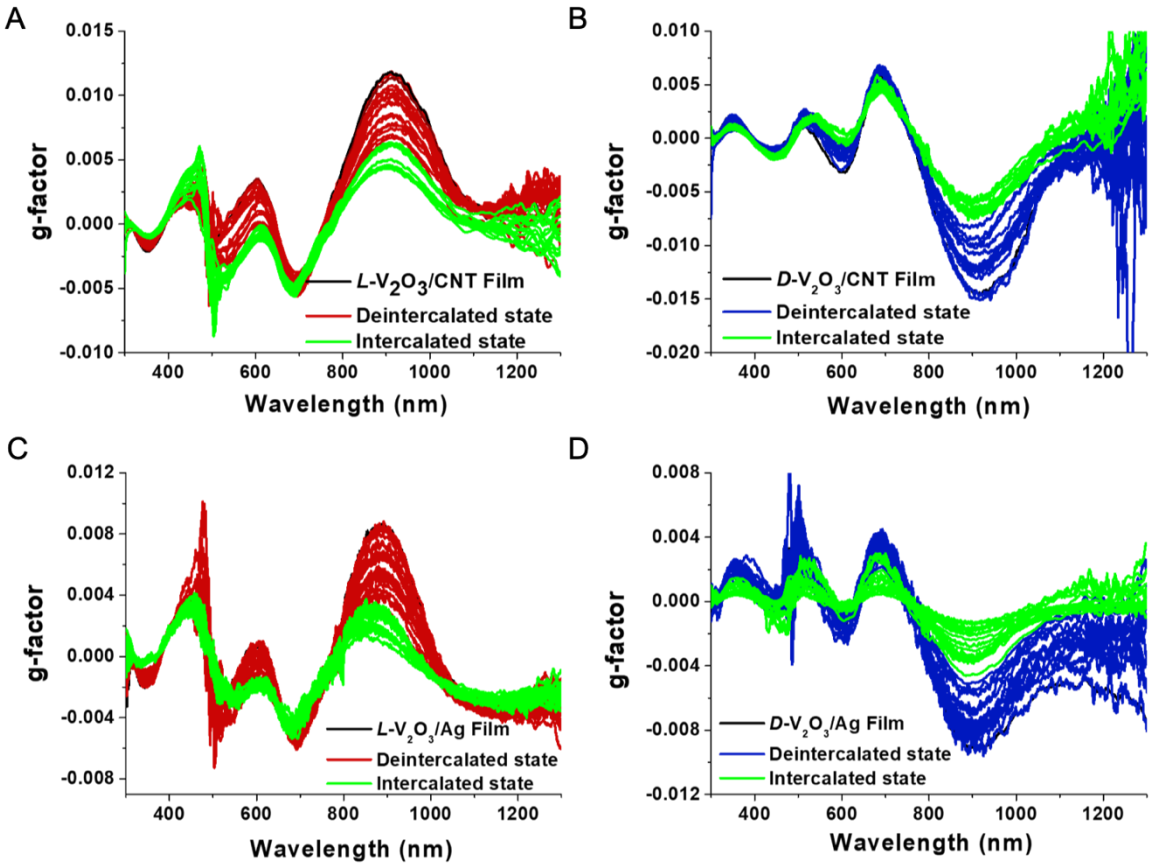

Figure S31. (A and B) Optical asymmetry *g*-factor spectra of *L*- and *D*-V_2O_3/CNT films, (C and D), *g*-factor spectra of *L*- and *D*-V_2O_3/Ag NWs films.

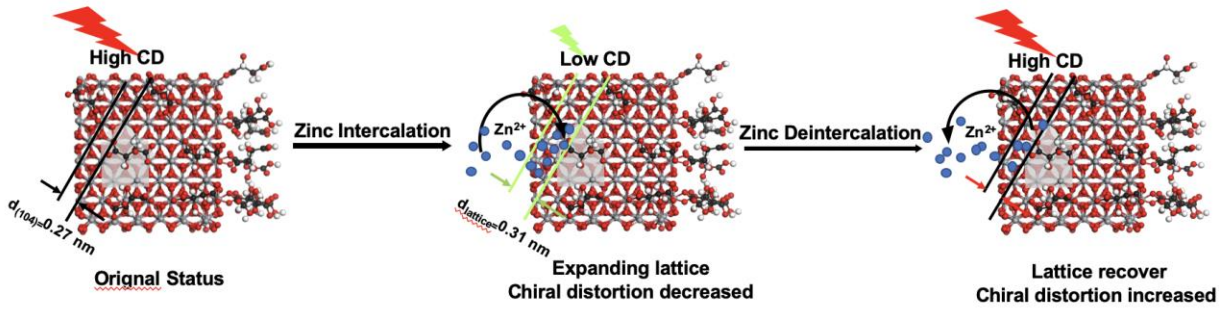

Figure S32. Illustration of CD reversibility and Zn^{2+} storage mechanism upon electrochemical intercalation and deintercalation processes.

References and Notes

1. Hausbrand, R. *et al.* Fundamental degradation mechanisms of layered oxide Li-ion battery cathode materials: Methodology, insights and novel approaches. *Mater. Sci. Eng. B* **192**, 3–25 (2015).

2. Yeom, J. *et al.* Chiromagnetic nanoparticles and gels. *Science (80-.).* **359**, 309–314 (2018).

3. Knoppe, S. & Bürgi, T. Chirality in thiolate-protected gold clusters. *Acc. Chem. Res.* **47**, 1318–26 (2014).

4. Wang, P.-P., Yu, S.-J., Govorov, A. O. & Ouyang, M. Cooperative expression of atomic chirality in inorganic nanostructures. *Nat. Commun.* **8**, 14312 (2017).

5. Wang, Z. *et al.* Origami-Based Reconfigurable Metamaterials for Tunable Chirality. *Adv. Mater.* **29**, 1–7 (2017).

6. Choi, W. J. *et al.* Terahertz circular dichroism spectroscopy of biomaterials enabled by kirigami polarization modulators. *Nat. Mater.* **18**, (2019).

7. Kuzyk, A. *et al.* A light-driven three-dimensional plasmonic nanosystem that translates molecular motion into reversible chiroptical function. *Nat. Commun.* **7**, 10591 (2016).

8. Fernandez-Corbaton, I. *et al.* New Twists of 3D Chiral Metamaterials. *Adv. Mater.* **31**, 1807742 (2019).

9. Wang, S. *et al.* Guanosine Assembly Enabled Gold Nanorods with Dual Thermo-and Photoswitchable Plasmonic Chiroptical Activity. *ACS Nano* **14**, 6087–6096 (2020).

10. Gansel, J. K. *et al.* Gold helix photonic metamaterial as broadband circular polarizer. *Science* **325**, 1513–5 (2009).

11. Suo, Z. *et al.* Highly Chiroptical Detection with Gold–Silver Bimetallic Nanoclusters Circularly Polarized Luminescence Based on G-quartet Nanofiber Self-assembly. *J. Phys. Chem. C* **124**, 21094–21102 (2020).

12. Zhang, S. *et al.* Photoinduced handedness switching in terahertz chiral metamolecules. *Nat. Commun.* **3**, 942 (2012).

13. Wu, G. *et al.* Optical absorption edge evolution of vanadium pentoxide films during lithium intercalation. *Thin Solid Films* **485**, 284–289 (2005).

14. Zhang, W., Li, H., Al-Hussein, M. & Elezzabi, A. Y. Electrochromic Battery Displays with Energy Retrieval Functions Using Solution-Processable Colloidal Vanadium Oxide Nanoparticles. *Adv. Opt. Mater.* **8**, 1901224 (2020).

15. Mjejri, I., Rougier, A. & Gaudon, M. Low-Cost and Facile Synthesis of the Vanadium Oxides V2O3, VO2, and V2O5 and Their Magnetic, Thermochromic and Electrochromic Properties. *Inorg. Chem.* **56**, 1734–1741 (2017).

16. Zheng, J. *et al.* V2O3/C nanocomposites with interface defects for enhanced intercalation pseudocapacitance. *Electrochim. Acta* **318**, 635–643 (2019).

17. Marini, C. *et al.* Optical properties of V 1− x Cr x O 2 compounds under high pressure. *Phys. Rev. B* **77**, 235111 (2008).

18. Heinz, H., Lin, T.-J., Kishore Mishra, R. & Emami, F. S. Thermodynamically Consistent Force Fields for the Assembly of Inorganic, Organic, and Biological Nanostructures: The INTERFACE Force Field. *Langmuir* **29**, 1754–1765 (2013).

19. Jung, S. H., Jeon, J., Kim, H., Jaworski, J. & Jung, J. H. Chiral arrangement of achiral Au nanoparticles by supramolecular assembly of helical nanofiber templates. *J. Am. Chem. Soc.* **136**, 6446–6452 (2014).

20. Dolamic, I., Varnholt, B. & Bürgi, T. Chirality transfer from gold nanocluster to adsorbate evidenced by vibrational circular dichroism. *Nat. Commun.* **6**, 7117 (2015).

21. Osipov, M. A., Pickup, B. T. & Dunmur, D. A. A new twist to molecular chirality: intrinsic chirality indices. *Molec. Phys.* **84**, 1193–1206 (1995).

22. Harris, A. B., Kamien, R. D. & Lubensky, T. C. Molecular chirality and chiral parameters. *Rev. Mod. Phys.* **71**, 1745–1757 (1999).

23. Kumar, P. *et al.* Photonically Active Bowtie Nanoassemblies with Chirality Continuum. *Res. Sq. [https//doi.org/10.21203/rs.3.rs-1614619/v1]* (2022).

24. Jiang, S. *et al.* Chiral ceramic nanoparticles and peptide catalysis. *J. Am. Chem. Soc.* **139**, 13701–13712 (2017).

25. Shelton, J. L. & Knowles, K. E. Thermally Activated Optical Absorption into Polaronic States in Hematite. *J. Phys. Chem. Lett.* **12**, 3343–3351 (2021).

26. Hao, C. *et al.* Chiral Semiconductor Nanoparticles for Protein Catalysis and Profiling. *Angew. Chemie - Int. Ed.* **58**, 7371–7374 (2019).

27. Yan, J. *et al.* Self-Assembly of Chiral Nanoparticles into Semiconductor Helices with Tunable near-Infrared Optical Activity. *Chem. Mater.* **32**, 476–488 (2020).

28. Ma, L., Cao, Y., Duan, Y., Han, L. & Che, S. Silver Films with Hierarchical Chirality. *Angew. Chemie Int. Ed.* **56**, 8657–8662 (2017).

29. Zhang, N. *et al.* Hydrated Layered Vanadium Oxide as a Highly Reversible Cathode for Rechargeable Aqueous Zinc Batteries. *Adv. Funct. Mater.* **29**, 1807331 (2019).

30. Kim, Y. *et al.* Reconfigurable chiroptical nanocomposites with chirality transfer from the macro-to the nanoscale. *Nat. Mater.* **15**, 461–468 (2016).

31. Probst, P. T. *et al.* Mechano-tunable chiral metasurfaces via colloidal assembly. *Nat. Mater.* **20**, 1024–1028 (2021).

32. Li, Z. *et al.* Reversible plasmonic circular dichroism of Au nanorod and DNA assemblies. *J. Am. Chem. Soc.* **134**, 3322–3325 (2012).

33. Wang, Y., Zhang, Y.-M. & Zhang, S. X.-A. Stimuli-Induced Reversible Proton Transfer for Stimuli-Responsive Materials and Devices. *Acc. Chem. Res.* **54**, 2216–2226 (2021).

34. Ariga, K., Hill, J. P. & Ji, Q. Layer-by-layer assembly as a versatile bottom-up nanofabrication technique for exploratory research and realistic application. *Phys. Chem. Chem. Phys.* **9**, 2319 (2007).

35. Zhao, S. *et al.* The Future of Layer-by-Layer Assembly: A Tribute to ACS Nano Associate Editor Helmuth Mohwald. *ACS Nano* **13**, (2019).

36. Yang, G., Li, Q., Ma, K., Hong, C. & Wang, C. The degradation mechanism of vanadium oxide-based aqueous zinc-ion batteries. *J. Mater. Chem. A* **8**, 8084–8095 (2020).

37. Shimazaki, Y., Mitsuishi, M., Ito, S. & Yamamoto, M. Preparation of the layer-by-layer deposited ultrathin film based on the charge-transfer interaction. *Langmuir* **13**, 1385–1387 (1997).

38. Yang, S. *et al.* Water uptake behavior of hydrogen-bonded PVPON–PAA LBL film. *Soft Matter* **2**, 699–704 (2006).

39. Shim, B. S. *et al.* Integration of conductivity, transparency, and mechanical strength into highly homogeneous layer-by-layer composites of single-walled carbon nanotubes for optoelectronics. *Chem. Mater.* **19**, 5467–5474 (2007).

40. Shim, B. S., Zhu, J., Jan, E., Critchley, K. & Kotov, N. A. Transparent conductors from layer-by-layer assembled SWNT films: importance of mechanical properties and a new figure of merit. *ACS Nano* **4**, 3725–34 (2010).

41. Cheng, G., Di, J. & Wang, Y. Chiroptical Study of Metal@ semiconductor–Molecule Composites: Interaction between Cysteine and Ag@ Ag3PO4 Core–Shell Hybrid Nanorods. *J. Phys. Chem. C* **119**, 22122–22130 (2015).

42. Jiu, J. *et al.* Facile synthesis of very-long silver nanowires for transparent electrodes. *J. Mater. Chem. A* **2**, 6326–6330 (2014).

43. Vanommeslaeghe, K., Raman, E. P. & MacKerell Jr, A. D. Automation of the CHARMM General Force Field (CGenFF) II: assignment of bonded parameters and partial atomic charges. *J. Chem. Inf. Model.* **52**, 3155–3168 (2012).

44. Vanommeslaeghe, K. *et al.* CHARMM general force field: A force field for drug-like molecules compatible with the CHARMM all-atom additive biological force fields. *J. Comput. Chem.* **31**, 671–90 (2010).

45. Crans, D. C. & Tracey, A. S. The Chemistry of Vanadium in Aqueous and Nonaqueous Solution. in *Vanadium Compounds* 2–29 (ACS Publications, 1998). doi:10.1021/bk-1998-0711.ch001.

46. Emami, F. S. *et al.* Force Field and a Surface Model Database for Silica to Simulate Interfacial Properties in Atomic Resolution. *Chem. Mater.* **26**, 2647–2658 (2014).

47. Banerjee, R., Mohanty, A., Chakravarty, S., Chakladar, S. & Biswas, P. A single-step process to leach out rare earth elements from coal ash using organic carboxylic acids. *Hydrometallurgy* **201**, 105575 (2021).

48. Mishra, R. K., Kanhaiya, K., Winetrout, J. J., Flatt, R. J. & Heinz, H. Force field for

calcium sulfate minerals to predict structural, hydration, and interfacial properties. *Cem. Concr. Res.* **139**, 106262 (2021).

49. Phillips, J. C. *et al.* Scalable molecular dynamics with NAMD. *J. Comput. Chem.* **26**, 1781–802 (2005).

50. Gowers, R. J. *et al. MDAnalysis: a Python package for the rapid analysis of molecular dynamics simulations*. (2019).

51. Michaud-Agrawal, N., Denning, E. J., Woolf, T. B. & Beckstein, O. MDAnalysis: a toolkit for the analysis of molecular dynamics simulations. *J. Comput. Chem.* **32**, 2319–2327 (2011).

52. Choi, J.-H. & Cho, M. Direct Calculations of Mid- and Near-IR Absorption and Circular Dichroism Spectra of Chiral Molecules Using QM/MM Molecular Dynamics Simulation Method. *J. Chem. Theory Comput.* **7**, 4097–4103 (2011).

53. Millar, G., Weinberg, N. & Mislow, K. On the Osipov–Pickup–Dunmur chirality index: why pseudoscalar functions are generally unsuitable to quantify chirality. *Mol. Phys.* **103**, 2769–2772 (2005).

54. Cha, M. *et al.* Unifying structural descriptors for biological and bioinspired nanoscale complexes. *Nat. Comput. Sci.* **2**, 243–252 (2022).

55. Ramírez, A. *et al.* Evaluation of MnO x, Mn2O3, and Mn3O4 electrodeposited films for the oxygen evolution reaction of water. *J. Phys. Chem. C* **118**, 14073–14081 (2014).

56. Mei, Y., Zhou, Z. & Luo, H. L. Electrical resistivity of rf-sputtered iron oxide thin films. *J. Appl. Phys.* **61**, 4388–4389 (1987).

57. Roy, T. K., Sanyal, D., Bhowmick, D. & Chakrabarti, A. Temperature dependent

resistivity study on zinc oxide and the role of defects. *Mater. Sci. Semicond. Process.* **16**, 332–336 (2013).

58. Kandalkar, S. G., Gunjakar, J. L., Lokhande, C. D. & Joo, O.-S. Synthesis of cobalt oxide interconnected flacks and nano-worms structures using low temperature chemical bath deposition. *J. Alloys Compd.* **478**, 594–598 (2009).

59. Jiang, H. *et al.* Ultrafine V2O3 nanowire embedded in carbon hybrids with enhanced lithium storage capability. *Ind. Eng. Chem. Res.* **54**, 2960–2965 (2015).

60. Kusano, E., Theil, J. A. & Thornton, J. A. Deposition of vanadium oxide films by direct-current magnetron reactive sputtering. *J. Vac. Sci. Technol. A Vacuum, Surfaces, Film.* **6**, 1663–1667 (1988).

61. Sarrigiannidis, S. O. *et al.* Chiral Tartaric Acid Improves Fracture Toughness of Bioactive Brushite–Collagen Bone Cements. *ACS Appl. Bio Mater.* **3**, 5056–5066 (2020).

62. Fu, B. *et al.* Interfacial interaction of tartaric acid with hydroxyapatite and enamel. *J. Mater. Sci. Mater. Med.* **16**, 827–831 (2005).

63. Gautier, C. & Bürgi, T. Chiral inversion of gold nanoparticles. *J. Am. Chem. Soc.* **130**, 7077–7084 (2008).

64. Rodríguez-Zamora, P. *et al.* Effect of the Metal–Ligand Interface on the Chiroptical Activity of Cysteine-Protected Nanoparticles. *Small* 2004288 (2021).

65. Tohgha, U. *et al.* Ligand induced circular dichroism and circularly polarized luminescence in CdSe quantum dots. *ACS Nano* **7**, 11094–102 (2013).

66. Moloney, M. P., Gun'ko, Y. K. & Kelly, J. M. Chiral highly luminescent CdS quantum

dots. *Chem. Commun.* **7345**, 3900 (2007).

67. Li, Y. *et al.* Tunable Chiroptical Properties from the Plasmonic Band to Metal–Ligand Charge Transfer Band of Cysteine-Capped Molybdenum Oxide Nanoparticles. *Angew. Chemie Int. Ed.* **57**, 10236–10240 (2018).

68. Cheng, J. *et al.* GoldHelix: Gold Nanoparticles Forming 3D Helical Superstructures with Controlled Morphology and Strong Chiroptical Property. *ACS Nano* **11**, 3806–3818 (2017).

69. Yeom, J. *et al.* Chiral supraparticles for controllable nanomedicine. *Adv. Mater.* **32**, 1903878 (2020).